Tellus SERIES A DYNAMIC METEOROLOGY AND OCEANOGRAPHY
PUBLISHED BY THE INTERNATIONAL METEOROLOGICAL INSTITUTE IN STOCKHOLM

Large-scale dynamical influence of a gravity wave generated over the Antarctic Peninsula – regional modelling and budget analysis

By JOEL ARNAULT*, *Swedish Institute of Space Physics, Box 812, SE-981 28, Kiruna, Sweden*

(Manuscript received 12 December 2012; in final form 28 January 2013)

ABSTRACT

The case study of a mountain wave triggered by the Antarctic Peninsula on 6 October 2005, which has already been documented in the literature, is chosen here to quantify the associated gravity wave forcing on the large-scale flow, with a budget analysis of the horizontal wind components and horizontal kinetic energy. In particular, a numerical simulation using the Weather Research and Forecasting (WRF) model is compared to a control simulation with flat orography to separate the contribution of the mountain wave from that of other synoptic processes of non-orographic origin. The so-called differential budgets of horizontal wind components and horizontal kinetic energy (after subtracting the results from the simulation without orography) are then averaged horizontally and vertically in the inner domain of the simulation to quantify the mountain wave dynamical influence at this scale. This allows for a quantitative analysis of the simulated mountain wave's dynamical influence, including the orographically induced pressure drag, the counterbalancing wave-induced vertical transport of momentum from the flow aloft, the momentum and energy exchanges with the outer flow at the lateral and upper boundaries, the effect of turbulent mixing, the dynamics associated with geostrophic re-adjustment of the inner flow, the deceleration of the inner flow, the secondary generation of an inertia–gravity wave and the so-called baroclinic conversion of energy between potential energy and kinetic energy.

Keywords: atmospheric modelling, budget analysis, gravity wave, momentum forcing, turbulence

1. Introduction

1.1. Review of past studies

It is well acknowledged that gravity waves originating either from topography, convection, wind shear, geostrophic adjustment, body forcing or wave–wave interaction significantly influence the dynamics of the large-scale atmospheric circulation (e.g. Fritts and Alexander, 2003). In earlier studies (e.g. Lilly, 1972), this effect was quantified in the spatially averaged equation of horizontal momentum by the vertical divergence of the so-called Reynolds stresses, that is, eddy vertical flux of horizontal momentum,

$$(X_{GW}, Y_{GW}) = -\frac{1}{\overline{\rho}} \cdot \frac{\partial}{\partial z} \left[\overline{\rho} \cdot \left(\overline{u'w'}, \overline{v'w'} \right) \right] \qquad (1)$$

where ρ is the air density, u the zonal wind, v the meridional wind, w the vertical velocity, $\partial/\partial z$ the partial derivate with respect to the vertical coordinate z, — a spatial averaging operator and $'$ the departure from this average. Indeed, for an adequately chosen averaging operator, X_{GW} and Y_{GW} are the terms through which gravity waves influence the mean flow.

Durran and Klemp (1995) investigated this effect for a two-dimensional numerical experiment of an orographically induced gravity wave, this idealised case being representative of the wave-breaking event observed over the Colorado Rockies on 17 February 1970 (Lilly and Kennedy, 1973). This idealised mountain had a height and width of 2 and 40 km, respectively, and the simulated domain's width (depth) was 500 (24) km with a horizontal (vertical) resolution of 1 km (stretched from 300 to 100 m). The idealised mountain wave was then triggered by westerlies blowing from the surface to the lower stratosphere (from 10 ms^{-1} at the surface to 50 ms^{-1} in the upper-tropospheric jet), and was breaking in the lower stratosphere, in association with convective overturning, enhanced turbulent dissipation and eventually momentum deposition. Horizontally averaging the terms of the horizontal momentum equation on the 500-km domain width,

*Correspondence.
email: joel.arnault@yahoo.fr

Citation: Tellus A 2013, **65**, 20254, http://dx.doi.org/10.3402/tellusa.v65i0.20254

that is, making a budget of horizontal momentum, Durran and Klemp (1995) found enhanced negative values of the averaged vertical divergence of eddy vertical flux of horizontal momentum [terms X_{GW} and Y_{GW} of eq. (1)] at breaking heights, although no remarkable decrease was found in the averaged tendency of horizontal momentum, that is, no deceleration was found due to the balancing contribution of averaged pressure force and horizontal divergence of horizontal momentum flux (the Coriolis effect was neglected). Indeed, in a control simulation with a 900-km domain width and periodic lateral boundary conditions, Durran and Klemp (1995) showed that the momentum deposition by the gravity wave had occurred outside of a 300-km width box around the mountain, suggesting that the terrain-induced perturbations in the pressure and horizontal velocity fields were rapidly transmitted hundreds of kilometres away from the mountain. It was thus proposed that at the horizontal scale of 400 km, that is, the large scale at which gravity waves are not resolved, the forcing term of eq. (1) as well as the wave-induced pressure force and horizontal divergence of horizontal momentum flux should all be considered to properly describe the large-scale effect of mountain wave propagation and breaking.

Following Durran and Klemp (1995), Héreil and Stein (1999) also considered a two-dimensional case study of a mountain wave, with an idealised mountain height (width) of 667 m (30 km), a simulated domain width (depth) of 4000 (12) km with a horizontal (vertical) resolution of 4 km (333 m), a uniform mean wind speed of 8 m s^{-1} and periodic lateral boundary conditions. The triggered mountain wave was breaking above the mountain, in association with convective overturning and enhanced turbulence. To study the eventual momentum deposition associated with this idealised mountain wave, Héreil and Stein (1999) also conducted a budget of horizontal momentum by integrating and normalising the terms of the equation of horizontal momentum horizontally for various box sizes, and vertically from the ground to a variable altitude, so that they could display vertical profiles of the terms of the budget. The advantage of the vertical integration was to separate the contribution of the so-called cross-mountain pressure drag from the averaged pressure work (by commuting the horizontal derivate and vertical integration operators). Indeed, this pressure drag quantifies the direct decelerating effect of topography on the mean flow, while gravity waves counterbalance this low-level sink, at least partially, by extracting and transporting downward horizontal momentum from the flow aloft (e.g. Durran and Klemp, 1995). For both integrated budgets of horizontal momentum with horizontal box sizes of 140 and 800 km, Héreil and Stein (1999) obtained that the decelerating pressure drag took place below 1000 m, in association with enhanced vertical divergence of eddy vertical flux of horizontal momentum and turbulent transport depleting and creating (creating and depleting) positive horizontal momentum above (below) 1000 m, while the pressure force and horizontal divergence of horizontal momentum flux partially counterbalanced these horizontal momentum transfer. For the 140-km box in particular, the resulting effect on the horizontal momentum tendency was almost negligible, except for a slight acceleration (deceleration) below (above) 1000 m. And for the 800-km box, the flow was much more decelerated between 1000 and 3000 m, slightly accelerated above. This decelerating (accelerating) effect below (above) 3000 m was also visible for 800-km boxes downstream and upstream the mountain, where the pressure drag, vertical divergence of eddy vertical flux of horizontal momentum and turbulent transport were negligible and the horizontal momentum tendency was essentially driven by the pressure force and horizontal divergence of horizontal momentum flux. Thus, Héreil and Stein (1999) confirmed the remote effect of the wave-induced pressure force and horizontal divergence of horizontal momentum flux suggested by Durran and Klemp (1995) [the Coriolis effect was also neglected in Héreil and Stein (1999)].

In a control simulation with open lateral boundary conditions, Héreil and Stein (1999) found a similar forcing due to the orographically induced gravity wave, that is, pressure drag, vertical divergence of eddy vertical flux of horizontal momentum and turbulent transport, but a negligible tendency of horizontal momentum when integrating vertically above 6000 m, due to counterbalancing horizontal divergence of pressure and horizontal momentum flux. Indeed with open lateral boundary conditions, the incident flow remains constant, resulting in adjusting pressure and horizontal momentum flux at the lateral boundaries to prevent a global mean flow deceleration in the simulated domain. This suggests that regional modelling allows quantifying the source terms due to the simulated gravity wave, but not its averaged impact on the large-scale flow, at least at the scale of the simulated domain.

Three-dimensional dynamics associated with gravity wave breaking in a non-rotating atmosphere has been addressed by Fritts et al. (1999) in a dimensionless idealised case study of a gravity wave propagating and convectively overturning in a three-dimensional geophysical flow characteristic of the middle atmosphere. These authors were particularly interested in the vorticity dynamics accompanying the transition from laminar to turbulent flow and obtained that streamwise counter-rotating vortices developed through baroclinic vorticity generation within the convectively unstable phase of the wave. These vortices further developed through vortex tilting and stretching,

resulting in a rapid cascade of energy toward smaller scales of motion.

Mountain wave effects on the mean flow circulation in a rotating atmosphere have been investigated in a three-dimensional idealised case study by Chen et al. (2007). Their idealised mountain was 1.5 km high with a horizontal size of about 200 km (40 km) north–south (east–west), and the simulated domain's width/length (depth) was 1800 km $\times$ 1800 km (18 km) with a horizontal (vertical) resolution of 6 km (stretched from 150 to 500 m). The idealised mountain wave was triggered by an idealised barotropic wave in a uniform westerly flow, with zonal velocities varying from 0 to 20 m s^{-1}. The lateral boundary conditions were periodic. A two-way-nested inner domain surrounding the mountain at 2 km horizontal resolution has been added to better represent the Ertel potential vorticity (PV) production by sub-grid turbulence associated with mountain wave breaking, and to take into account this PV production in the outer domain, that is, on the large-scale flow. The idealised mountain wave was breaking right above the mountain in association with convective overturning, enhanced turbulence, shedding counter-rotating vortices, deceleration of zonal winds in a central west–east corridor downstream of the mountain and patches of accelerated zonal winds south and north of this corridor, as deduced after comparison with a control simulation in which the mountain was removed. Chen et al. (2007) characterised the shedding counter-rotating vortices with PV anomalies, these last ones accounting for most of the wave-induced wind disturbances as deduced from PV inversion. The generation of these PV anomalies was then related to persistent turbulent mixing occurring in the lee of the mountain during gravity wave breaking, after which the PV anomalies were passively advected downstream by the synoptic-scale flow. However, the horizontally averaged winds in the 1800 km $\times$ 1800 km domain showed weak fluctuations, of the order of 10^{-1} m s^{-1}, suggesting these PV anomalies did not modify much the 1800 km large-scale flow and that the mountain-induced circulations were primarily redistributing momentum inside the 1800 km $\times$ 1800 km domain. Nevertheless, Chen et al. (2007) showed that these fluctuations of averaged wind were inertial oscillations triggered by vertical divergence of eddy vertical fluxes of horizontal momentum, that is, the gravity-wave-forcing terms X_{GW} and Y_{GW} in eq. (1), and that these oscillations were maxima below 8 km where the mountain wave was breaking, weaker but still present above.

The dynamical influence of gravity waves on the mean flow can also be quantified with the divergence of the Eliassen-Palm (EP) flux, or wave activity flux, in the transformed Eulerian-mean (TEM) equations, a theory originally developed by Andrews and McIntyre (1976) to quantify the impact of planetary waves on the mean zonal circulation. For example, Watanabe et al. (2008) used EP flux divergence to quantify the effect of the resolved atmospheric waves in a 3-yr simulation with a general circulation model characterised by a horizontal resolution of about 60 km and 256 vertical levels up to 85 km altitude with a uniform spacing of 350 m. The particular contribution of gravity waves, including those of orographic origin, was diagnosed by extracting waves with the highest wave numbers (>42) and evaluating the associated EP flux divergence. From this analysis, Watanabe et al. (2008) concluded that the modelled gravity waves caused deceleration of the wintertime polar westerly jet in the upper stratosphere and of the summertime easterly jet in the mesosphere for the simulated 3-yr period.

Kinoshita et al. (2010) derived a version of TEM equations including a three-dimensional residual mean circulation, the mean operator being applied either on time or space at any scale, thus being less restrictive than the zonal mean used in Andrews and McIntyre (1976), although the scale of the mean operator still has to be large enough to assume hydrostatic balance. Besides the divergence of the wave activity flux, that is, the EP flux, gravity waves also impact the TEM equations through the advection of the mean flow by the three-dimensional residual mean circulation, which can be related to the advection of the mean flow by the Lagrangian-mean circulation (as in Andrews and McIntyre, 1976). The TEM equations are therefore adapted to study the influence of gravity waves on the transport of mean tracers in the atmosphere. In particular, Kinoshita et al. (2010) addressed the three-dimensional transport of time-mean ozone in the Southern Hemisphere using data from a Chemistry Climate Model. They found that the divergence (convergence) of the three-dimensional wave activity flux was mainly balanced by the product of the Coriolis parameter and the strong poleward (equatorward) Stokes drifts, that is, the difference between the Lagrangian-mean flow and the Eulerian-mean flow, thus suggesting gravity waves play a role in meridional ozone transport.

1.2. Outline of the present work

Continuing the horizontal momentum budget analyses done by Durran and Klemp (1995) and Héreil and Stein (1999) for quantifying the dynamical influence of mountain waves on the mean flow in idealised numerical experiments, it is proposed here to conduct a comparable budget analysis for a real-case numerical experiment, using the Weather Research and Forecasting (WRF; Skamarock and Klemp, 2008) model. Since WRF resolves the Eulerian equations of momentum, the mountain wave forcing in the Eulerian-mean budget of horizontal momentum can be

extracted by comparing with a control simulation in which the orography has been removed (e.g. Arnault and Kirkwood, 2012), as will be shown in the following. The Lagrangian point of view [using the TEM equations, for example, Kinoshita et al. (2010)] certainly brings an interesting point of view on the physical processes at stake, although this topic won't be addressed in the present article and is left for future research.

The real-case study chosen here is the gravity wave triggered by the Antarctic Peninsula on 6 October 2005 (referred to as the 'AP gravity wave' in the following) that has already been documented by Plougonven et al., 2008. In their work, a WRF model experiment of this AP gravity wave was compared with wind and temperature measurements from long duration balloon flights and radiosounding, and analyses from the European Center for Medium-Range Weather Forecasts (ECMWF). Assessed by the measurements, their WRF simulation brought further evidence that the wave was breaking in the lower stratosphere, in association with a deposition of momentum in the opposite direction to the mean westerly flow as deduced from an estimation of eddy vertical fluxes of horizontal momentum in eq. (1), and a generation of a secondary inertia–gravity wave in the lower stratosphere. The large-scale atmospheric circulation associated with this AP gravity wave is briefly reviewed in section 2, a WRF modelling experiment, similar to that of Plougonven et al. (2008), with and without orography is presented in section 3, a budget analysis of the horizontal wind components u and v and horizontal kinetic energy $K_H = 0.5*(u^2+v^2)$ is carried out in section 4, and some conclusions are given in section 5.

2. Synoptic situation of the Antarctic Peninsula gravity wave of 6 October 2005

Following Plougonven et al. (2008), ECMWF operational analyses are used here to document the synoptic situation in which the AP gravity wave took place. As already shown by Plougonven et al. (2008), a low pressure centre moving eastward and centered around (100°W, 65°S) on 6 October 2005 induced enhanced northwesterly winds on the northern side of the trough blowing over the peninsula. The horizontal cross section at 5 km altitude of vertical velocity and horizontal winds on 1800 UTC 6 October 2005 (Fig. 1) illustrates these meteorological conditions and shows that the AP gravity wave is already resolved in the ECMWF analyses (see the elongated strips of negative/positive vertical velocities of order of magnitude ± 0.2 m s^{-1} along the Antarctic Peninsula and perpendicular to the winds) although it does not propagate above 10 km in these data (not shown).

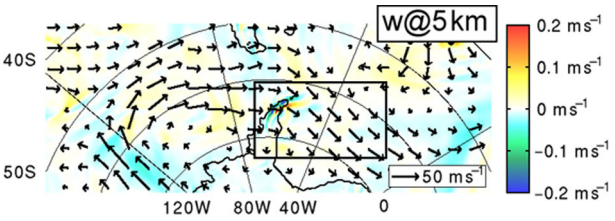

Fig. 1. Projection on the WRF outer domain of vertical velocity (colour) and horizontal winds (arrows) in m s^{-1}, computed with ECMWF operational analyses at 5000 m altitude on 1800 UTC 6 October 2005. The vertical velocity scale is given by the coloured bar to the right and the wind scale by the arrow at the bottom right corner. Black contours indicate the coast of the Antarctic continent and South America. The black box around the Antarctic Peninsula gives the location of the inner domain used in the WRF simulation, which is also the domain used in the domain- and box-averaged budget analysis of Figs. 9–14.

Since Plougonven et al. (2008) found evidence that the AP gravity wave was propagating in the stratosphere and depositing momentum there, the large-scale stratospheric circulation associated with this wave is also investigated here with ECMWF analyses. In particular, Fig. 2 provides three horizontal cross sections of pressure and winds at 15, 25 and 35 km altitude on 1800 UTC 6 October 2005. It shows that stratospheric winds were mainly zonal above the Antarctic Peninsula when the AP gravity wave took place, related to a well-defined polar vortex at that time. The following section presents WRF numerical experiments, with and without orography, which will be used to quantify the influence of the AP gravity wave on this large-scale circulation.

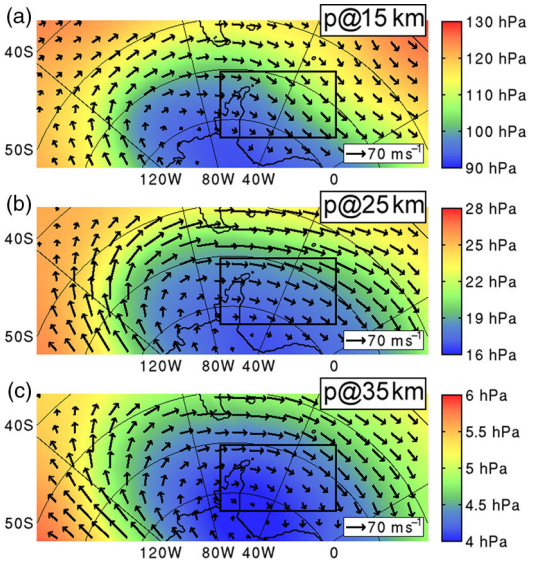

Fig. 2. As in Fig. 1, except for the pressure in hPa at isoaltitudes 15000 m (a), 25000 m (b) and 35000 m (c).

3. Numerical simulation

3.1. About the Weather Research and Forecasting model

The WRF model (Skamarock and Klemp, 2008) resolves the non-hydrostatic compressible equations of motion in their flux form using a terrain-following hydrostatic pressure (mass) vertical coordinate $\eta = (p_h - p_{ht})/(p_{hs} - p_{ht}) = (p_h - p_{ht})/\mu$, where p_h is the hydrostatic pressure, p_{ht} and p_{hs} are the hydrostatic pressures at the top and surface of the model, respectively, and $\mu = p_{hs} - p_{ht}$ represents the mass of the dry air per unit area within the column in the model domain. In this mass-coordinate system, the three-dimensional components of the momentum are defined as $U = \mu u$, $V = \mu v$ and $W = \mu w$, where u, v and w are the three-dimensional components of the wind. More particularly the flux-form equations of U and V solved in the WRF model can be written as follows:

$$\underbrace{\frac{1}{\mu}U_t}_{\text{2a:Budgetu\_tend}} = \underbrace{-\frac{1}{\mu}\left[(Uu)_x+(Vu)_y+(\Omega u)_\eta\right]}_{\text{2b:Budgetu\_divfluxt}} \underbrace{-\alpha\left(p_x-\frac{\Phi_x}{\Phi_\eta}p_\eta\right)}_{\text{2c:Budgetu\_pres}} \underbrace{+f\cdot v}_{\text{2d:Budgetu\_cori}} \underbrace{+F_u}_{\text{2e:Budgetu\_fric}} \tag{2}$$

$$\underbrace{\frac{1}{\mu}V_t}_{\text{3a:Budgetv\_tend}} = \underbrace{-\frac{1}{\mu}\left[(Uv)_x+(Vv)_y+(\Omega v)_\eta\right]}_{\text{3b:Budgetv\_divfluxt}} \underbrace{-\alpha\left(p_y-\frac{\Phi_y}{\Phi_\eta}p_\eta\right)}_{\text{3c:Budgetv\_pres}} \underbrace{-f\cdot u}_{\text{3d:Budgetv\_cori}} \underbrace{+F_v}_{\text{3e:Budgetv\_fric}} \tag{3}$$

with

$$\Omega = \frac{1}{\Phi_\eta}\left(g\cdot W - \Phi_x U - \Phi_y V\right) \tag{4}$$

where U, V and Ω are the contravariant components of the momentum in the coordinate system of the model (x, y, η), subscripts x, y, η and t stand for the derivate operators in the three directions of this coordinate system and the time derivate operator, Φ is the geopotential, g the acceleration of gravity, α the specific volume of the moist air, p the atmospheric pressure, f the Coriolis parameter and F_u and F_v the horizontal components of the frictional forces. In eq (2/3), the tendency of U/V (2a/3a) is the sum of the total divergence of U/V fluxes (2b/3b), the pressure force (2c/3c), the Coriolis force (2d/3d) and the frictional dissipation (2e/3e). The curvature term and the Coriolis component depending on vertical velocity, that are actually resolved in the model, have been omitted in eq (2) and eq. (3) since their contribution have been found to be negligible in the budget analysis of section 4.

It has to be noted here that the WRF model does not resolve explicitly the usual form of momentum in the height coordinate, that is, density times wind, but the vertically integrated mass μ times wind. Klemp et al. (2007) made several idealised and real case modelling experiments with the non-hydrostatic compressible equations using terrain following either mass or height coordinates, and concluded that the two coordinate systems produce very comparable results, both on a case-by-case basis and statistically. The mass-coordinate system has been chosen for the operational version of the WRF model (Skamarock and Klemp, 2008), the one used here, since a constant pressure upper surface allows the atmosphere to expand or contract vertically in response to heating and cooling, which allows a more realistic response to diabatic processes in comparison to the height coordinate with a rigid upper surface in which heating can produce artificial pressure increases or mass removal (Klemp et al., 2007).

When averaging eq. (2) and eq. (3) in the budget analysis of section 4, it has been found that $U_t/\mu = u_t$ and $V_t/\mu = v_t$ with an accuracy above two orders of magnitude. This means that in the present case the budget of horizontal momentum U and V, as defined in the WRF model, actually provides a budget of the horizontal wind components u and v, such as in a typical pressure coordinate system but without the assumption of hydrostatic balance (Klemp et al., 2007). In other words, averaged eq. (2/3) equalise the averaged tendency of u/v (2a/3a) to the sum of the averaged total divergence of U/V fluxes (2b/3b), the averaged pressure force (2c/3c), the averaged Coriolis force (2d/3d) and the averaged frictional dissipation (2e/3e), at least in the model experiment presented here. Since the present article aims at quantifying the dynamical influence of the AP gravity wave on the large-scale circulation, that is, large-scale winds, a budget of u and v deduced from averaged eq. (2) and eq (3) in a WRF model experiment is certainly well adapted for that purpose.

3.2. Setting of the experiment

Plougonven et al. (2008) simulated the AP gravity wave with the WRF model from 1200 UTC 5 October 2005 to 1800 UTC 7 October 2005, using two nested domains of horizontal resolutions 21 and 7 km, 112 vertical levels and a model top at 1 hPa. Similarly to that, the WRF simulations with and without orography presented here consist of two nested polar stereographic outer and inner domains of horizontal size (south–north × east–west in km) 3600×9000 and 1500×2580, and horizontal resolutions 30 and 6 km, respectively (see Fig. 1 for the location of the outer and inner domains). It has to be noted here

that the chosen inner domain's horizontal size and resolution are similar to those in the idealised case study by Chen et al. (2007). For the simulation with orography, the terrain elevation of the inner domain is given in Fig. 3, showing a mountain ridge up to 2000 m altitude and about 50 km wide along the western side of the Antarctic Peninsula, which is comparable to the idealised mountain's size used in the two- (three-) dimensional case study of mountain wave by Durran and Klemp, (1995) and Chen et al. (2007). The model equations are then integrated at a time step of 120 and 24 s for the outer and inner domains, respectively, and the inner domain outputs containing the usual dynamic and thermodynamic variables, as well as the time-integrated terms of the budgets of u, v and K_H presented in section 4, are saved every 20 min.

In the simulation with orography, the inner domain is aimed at resolving small-scale processes associated with the AP gravity wave, while the outer domain has been chosen large enough to resolve the large-scale circulation eventually influenced by the AP gravity wave. Indeed both Durran and Klemp (1995) and Héreil and Stein (1999) suggested that gravity waves influence the large-scale circulation remotely, with some quantitative effect only appearing beyond 100 and still visible 1000 km away from the mountain. A two-way grid-nesting is used in order to resolve the scale interactions between the inner and outer domains, so that a budget analysis in the inner domain won't be affected by fixed lateral boundary conditions as pointed out by Héreil and Stein (1999). Both outer and inner domains have 153 vertical levels up to 1 hPa (approximately 45 km in this case), with a vertical spacing stretched from 60 m to 400 m at the lowest and highest level, respectively. Rayleigh damping in the uppermost 5 km is introduced in order to avoid spurious wave reflection from the model lid (following Durran and Klemp, 1983).

The two numerical experiments start on 0000 UTC 6 October 2005 and are run for 1 d—the two nested domains being initialised by ECMWF operational analyses and the outer domain being coupled with these analyses at its lateral boundaries every 6 hours. The general idea of the present work is to quantify how the simulated circulation without orography diverges from the one with orography, so that a 1-d simulation is sufficient for that purpose, as shown later. More over, according to Plougonven et al. (2008), low-level westerlies blew on the Antarctic Peninsula from 1 October 2005 and for a two-week period. This means that the WRF simulation of the AP gravity wave presented here will start with a transition period during which the gravity wave fluctuations provided by the ECMWF analyses at the initial time will adjust to the finer resolution of the model. This artefact may affect the realism of the simulated AP gravity wave in the beginning of the simulation, and consequently its impact of the large-scale simulated circulation, which will be further discussed in the budget analysis of section 4.

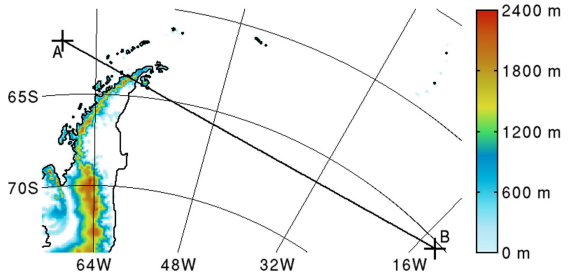

Fig. 3. Terrain elevation (m) of the inner domain used for the WRF simulation with orography. The height scale is given by the coloured bar to the right. The curved black line delimits the coast of the Antarctic Peninsula and off-shore islands. The straight black line (A–B) gives the location of the vertical cross-sections in Fig. 6.

Concerning the physics taken into account in the numerical experiment, convection is parameterised with the Kain–Fritsch cumulus scheme (Kain, 2004) in the outer domain, and it is explicit in the inner domain. Microphysics is parameterised with the 3-class liquid and ice hydrometeors scheme of Hong et al. (2004). Radiative processes are represented with the rapid radiation transfer model (rrtm) longwave radiation scheme (Mlawer et al., 1997) and with the Goddard shortwave radiation scheme (Chou and Suarez, 1994). Sub-surface heat conduction is calculated with a scheme based on a 5-layer soil temperature. Horizontal turbulent transport of heat, moisture and momentum is determined with a horizontal first order Smagorinsky closure, and the vertical turbulent transport of the same quantities is parameterised in the whole atmospheric column with the scheme of Hong et al. (2006).

3.3. *Qualitative results*

According to balloon measurement and radiosondes, Plougonven et al. (2008) obtained a realistic WRF simulation of the AP gravity wave from 1200 UTC 5 October to 1800 UTC 7 October. In particular, balloon measurements above the Antarctic Peninsula on 0600 UTC 7 October at 17–18 km altitude showed that at that time and location, the AP gravity wave was characterised by an intrinsic period of 45 min; oscillations in the u, v, w wind components of amplitude ± 15, 12.5, 2 ms^{-1}, respectively; and temperature oscillations of ± 17 K. From these observations, Plougonven et al. (2008) assumed that the AP gravity wave was a pure gravity wave, leading to horizontal and vertical wavelengths of 85 and 8 km, respectively. In their WRF simulation, the AP gravity wave had an intrinsic period of 28–34 min, assuming the stationarity of their modelled AP gravity wave and a

horizontal wind velocity perpendicular to the Antarctic Peninsula ridge of 30–35 ms^{-1}. Their modelled AP gravity wave was also characterised by a horizontal wavelength of 50–65 km; a vertical wavelength of 10–12 (8–10) km in the troposphere (lower stratosphere); lower stratospheric oscillations in the u, v, w components of the wind of amplitude $\pm$14–18, 14–18, 3–4 ms^{-1}, respectively; and of amplitude $\pm$15–20 K in the potential temperature field.

With the exception that in the WRF simulation of Plougonven et al. (2008), the inner domain's horizontal size was roughly six times smaller than the one used here, and their vertical resolution was slightly coarser above 20 km, the rest of the simulation's parameters were similar to those used here. Since Plougonven et al. (2008) also obtained realistic results, that is, similar to those described above, in a test simulation starting on 1200 UTC 6 October 2005, it is argued that the WRF experiment discussed here also gives a realistic representation of the AP gravity wave for the simulated 1-d period from 0000 UTC 6 October 2006, as shown below. It is then argued that the inner domain (Fig. 3) is large enough to resolve the dynamics of the secondary inertia–gravity wave generated by the breaking AP gravity wave in the lower stratosphere, as originally proposed by Plougonven et al. (2008).

Figures 4 and 5a display horizontal cross sections of vertical velocity at 5 and 30 km altitude, respectively, for the simulated inner domain on 1800 UTC 6 October 2005. These figures confirm that the AP gravity wave did propagate into the stratosphere, with vertical velocity oscillations of order of magnitude $\pm$2 m s^{-1}, a horizontal wavelength of about 30–60 km slightly increasing with height and a wave size also increasing with height. Assuming the stationarity of this modelled AP gravity wave and a horizontal wind velocity perpendicular to the

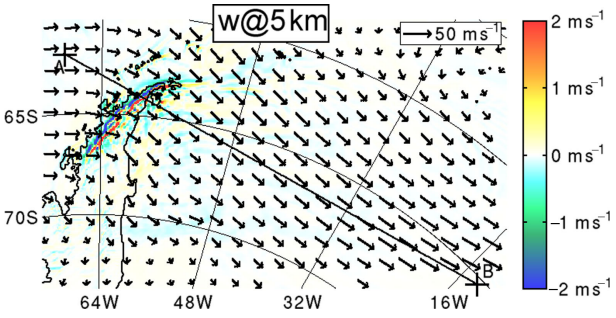

Fig. 4. Horizontal cross-section at 5-km altitude of vertical velocity (colour) and horizontal winds (arrows) in m s^{-1}, computed from the inner domain outputs of the WRF modelling experiment with orography on 1800 UTC 6 October 2005. The vertical velocity scale is given by the coloured bar on the right side and wind scale by the arrow on the bottom right corner of the panel. The straight black line (A–B) gives the location of the vertical cross sections in Fig. 6.

Antarctic Peninsula ridge of 30–35 ms^{-1} (as in Plougonven et al., 2008) give an intrinsic period of 14–34 min.

The corresponding vertical cross section of vertical velocity displayed in Fig. 6a shows that the AP gravity wave had a vertical wavelength of about 8 km in the troposphere, reduced to about 5 km in the stratosphere. Horizontal cross sections at 30 km altitude of the u and v components of the wind on 1800 UTC 6 October 2005 (Fig. 5b and 5c), as well as the associated vertical cross sections (Fig. 6b and 6c), reveal that the simulated horizontal wind has oscillating fluctuations similar to those previously discussed in the w component, with an amplitude of $\pm$15–25 ms^{-1} in both u and v components (Figs. 5a and 6a). The inertial property of these oscillations, as suggested by Plougonven et al. (2008), will be discussed in the next sections.

Since Plougonven et al. (2008) found that the AP gravity wave was breaking in the lower stratosphere, thus explaining the generation of a secondary inertia–gravity wave according to several observational and modelling studies (e.g. Scavuzzo et al., 1998; Vadas et al., 2003; Spiga et al., 2008), horizontal cross section of static stability N at 30 km altitude on 1800 UTC 6 October 2005 as well as the corresponding vertical cross section are represented in Figs. 5d and 6d, respectively. These two figures show that the oscillating pattern in w (Figs. 5a and 6d) is also present in N, so that the simulated AP gravity wave not only has a signature in the three components of the wind field, but also in the mass field. More over the negative phases of the oscillations in N lead to static instability in localised area (see the horizontally and vertically elongated blue strips in Figs. 5d and 6d between 25 and 35 km altitude), which are associated with enhanced turbulence as deduced by a Richardson number (RI) lower than 0.25 in Figs. 5e and 6e. It has to be noted here that Plougonven et al. (2008) obtained similar results from their WRF simulation of the AP gravity wave.

Since Chen et al. (2007) suggested in an idealised case study that enhanced turbulence induced by convective overturning during gravity wave breaking is responsible for the generation of PV anomalies passively advected downstream by the synoptic-scale flow, this whole process resulting in a momentum redistribution inside a 1800 km $\times$ 1800 km domain, it is proposed here to analyse the horizontal cross section of PV at 30 km altitude on 1800 UTC 6 October 2005 as well as the corresponding vertical cross section (Figs. 5f and 6f, respectively). It has to be noted here that PV values in the stratosphere are much stronger than what is usually observed in the troposphere ($\pm 10^3$ pvu at 30 km, $\pm 10^4$ pvu at 40 km), due to the effect of the polar vortex but also density. Therefore, it is the vertical cross section of ρPV, not of PV, that is shown in Fig. 6f, in order to distinguish the PV negative anomalies

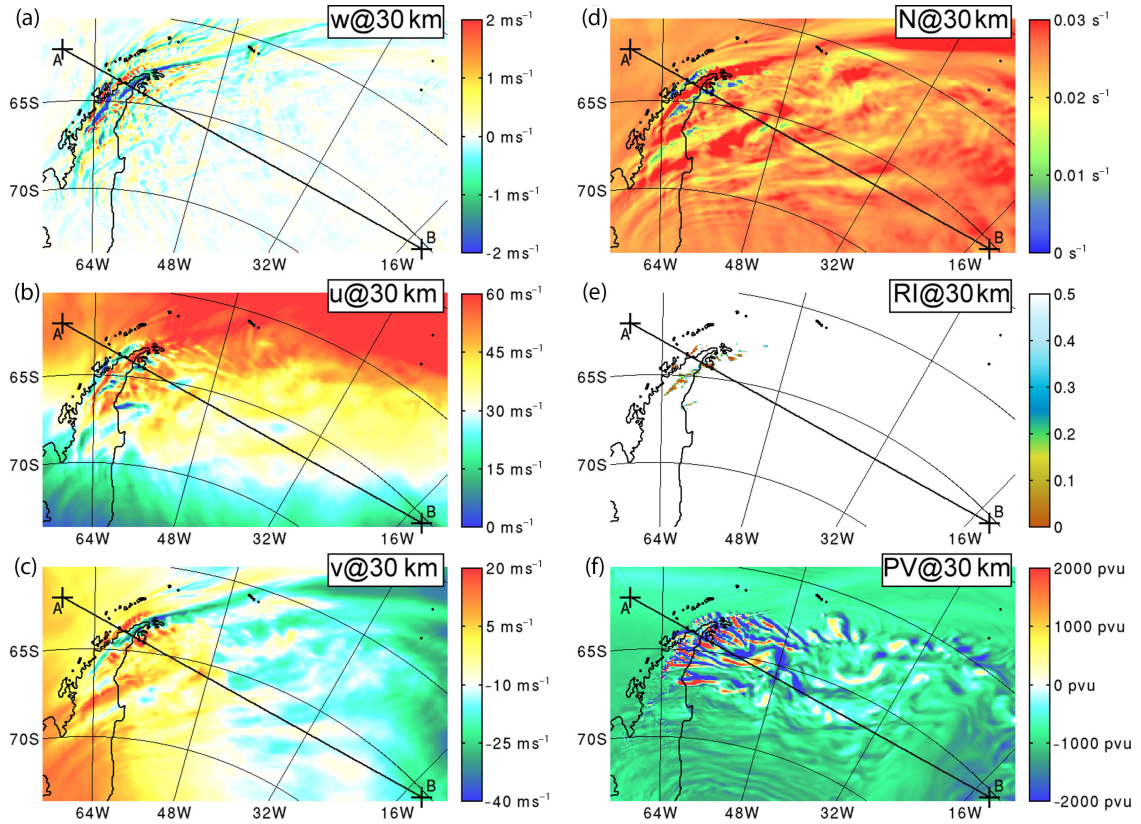

Fig. 5. (a) As in Fig. 4, except for the vertical velocity in m s^{-1} at 30 km altitude. (b) As in (a), except for the x-component of the wind in m s^{-1}. (c) As in (a), except for the y-component of the wind in m s^{-1} at 30 km altitude. (d) As in (a), except for the static stability in s^{-1}. (e) As in (a), except for the Richardson number. (f) As in (a), except for the potential vorticity in pvu.

from the negative background in the stratosphere (cf. negative vorticity for cyclonic circulation in the Southern Hemisphere). Figure 5f clearly shows streamwise counter-rotating vortices propagating downstream (shedding vortices) that could be generated in the model by enhanced turbulence at places where the AP gravity wave is convectively overturning (compare Fig. 5d–5f) as suggested by Chen et al. (2007). However, these PV anomalies could also result from vorticity dynamics involving baroclinic vorticity generation within the convectively unstable phase of the wave followed by vortex tilting and stretching (e.g. Fritts et al. 1999), since these source terms in the absolute vorticity equation are implicitly contained in the advection term of the PV equation. Therefore, Fig. 6f shows that these PV anomalies are mainly located above 15 km altitude and seem to result in an increase of the ambient cyclonic PV between 30 and 35 km and a decrease above these heights when comparing PV values upstream and downstream. This suggests that a quantitative analysis of the PV equation, and of the absolute vorticity equation also, would certainly complement the budget analysis of u, v and K_H of section 4 for studying the impact of the simulated AP gravity wave on the large-scale flow, although this has been left for a future work.

Since these qualitative results, and also those of Plougonven et al. (2008), suggest that the AP gravity wave did have some dynamical influence on its surrounding circulation, at least in the WRF simulation, this influence is now quantified by comparing with a control simulation in which the orography has been removed.

3.4. *Domain- and box-averaged analysis*

The AP gravity wave effect on the mean flow is further analysed with so-called domain-averaged quantities, that is, vertical profiles averaged horizontally in the inner domain (see the domain delimited by the black rectangle in Fig. 1), and so-called box-averaged quantities, that is, vertically integrated domain-averaged quantities. In particular, Fig. 7a–7c displays the time evolution of the domain-averaged u, v and K_H from the modelling experiment with orography, and Fig. 7d–7f displays the departure of these domain-averaged quantities from the

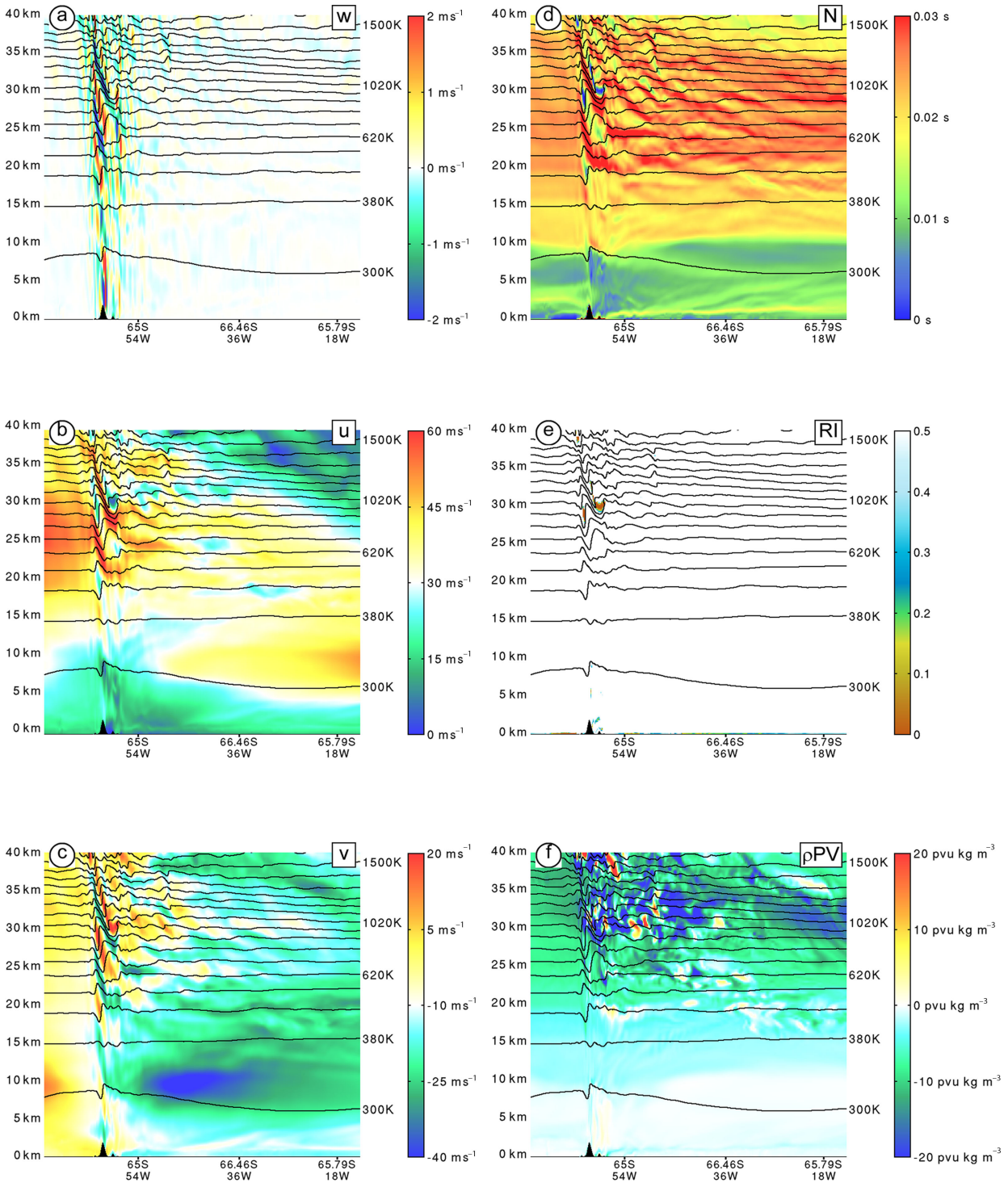

Fig. 6. (a) Vertical cross section of the vertical velocity (colour) in m s^{-1} and the isentropes (black contours) in K, computed from the inner domain outputs of the WRF modelling experiment with orography at the location indicated by line (A–B) in Figs. 3–5 on 1800 UTC 6 October 2005. The horizontal axis gives the horizontal coordinate in (latitude, longitude) and the vertical axis on the left-side (right side) gives the altitude in m (the potential temperature in K). The profile of the Antarctic Peninsula ridge is shaded in black. (b) As in (a), except for the x-component of the wind in m s^{-1}. (c) As in (a), except for the y-component of the wind in m s^{-1}. (d) As in (a), except for the static stability in s^{-1}. (e) As in (a), except for the Richardson number. (f) As in (a), except for the density times potential vorticity in pvu kg m^{-3}.

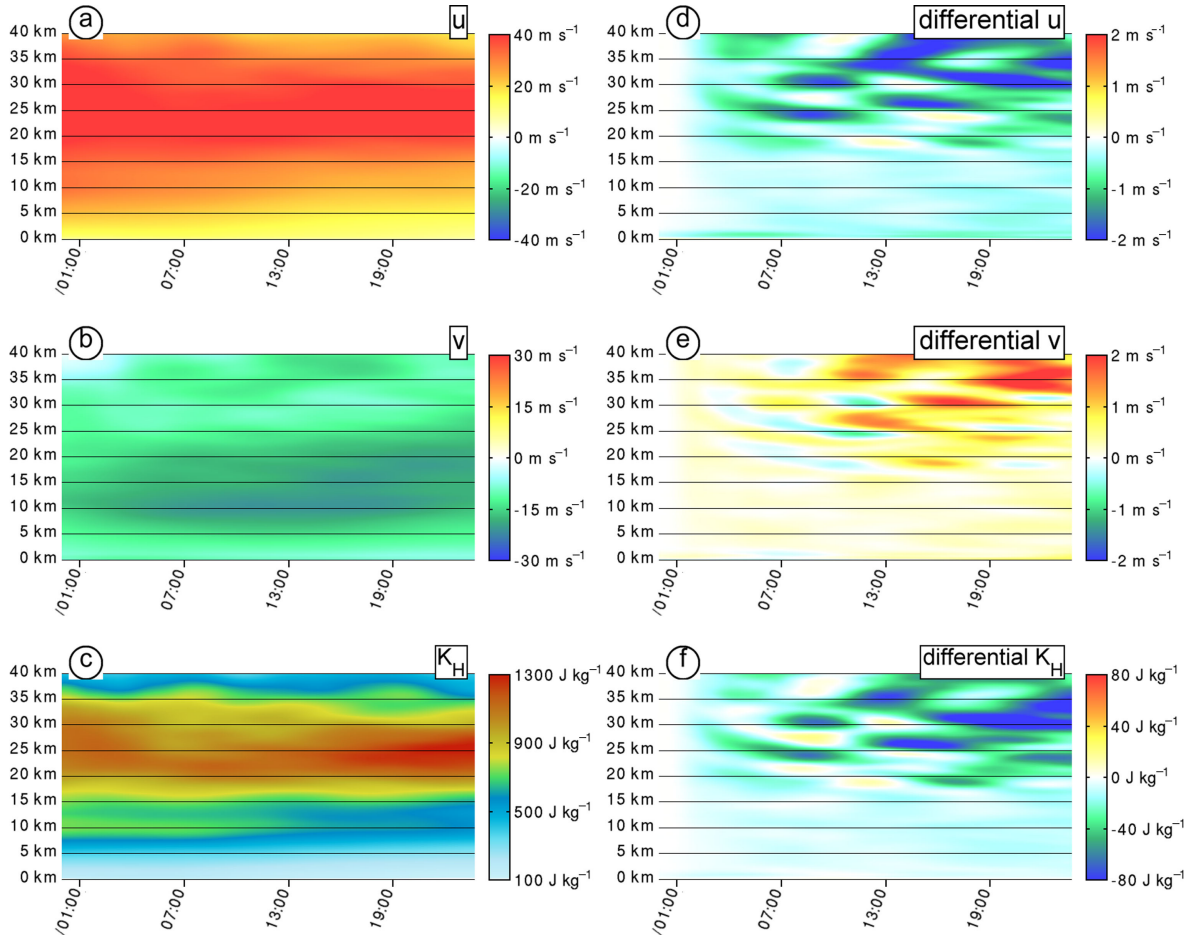

Fig. 7. (a) Time–height diagram of u in m s^{-1} from the 20-min inner domain outputs of the WRF model experiment with orography, domain-averaged in the inner domain (see the domain delimited by the black rectangle in Fig. 1). The horizontal axis gives the time in hours from 0000 UTC 6 October 2005 to 0000 UTC 7 October 2005 and the vertical axis gives the height in m. The wind scale is given by the coloured bar on the right hand of the panel. (b) As in (a), except for v in m s^{-1}. (c) As in (a), except for K_H in J kg^{-1}. (d) As in (a), except for the so-called differential u calculated as the difference between outputs from the WRF model experiments with and without orography. (e) As in (d), except for differential v. (f) As in (a), except for differential K_H.

results of the simulation without orography. As stated by Arnault and Kirkwood (2012), such a subtraction is assumed to remove the contribution from synoptic processes of non-orographic origin, so these so-called differential domain-averaged quantities display only the features associated with the AP gravity wave and other processes of orographic origin. It has to be noted here that the modelled AP gravity wave is associated with orographically induced convection that slightly modifies its amplitude and shape, as deduced from a comparison with a control simulation without cloud microphysics (not shown). In the following analysis the differential quantities displayed are therefore considered to represent the contribution of the AP gravity wave including moist convective effects.

Figures 7a and 7b shows that the domain-averaged wind has positive u and negative v components of comparable amplitude (around $\pm$30–50 ms^{-1}) both in the troposphere and stratosphere, since u and v are not zonal and meridional wind, respectively, but wind components on the stereographic projection (e.g. Fig. 3). The vertical profile of domain-averaged K_H (Fig. 7c) further shows that the simulated wind profile is characterised by a strong stratospheric jet of maximal intensity between 20 and 30 km altitude (around 1000 J kg^{-1} before noon, increasing to 1300 J kg^{-1} afterwards), which is part of the polar vortex identified in ECMWF analyses (Fig. 2).

The domain-averaged differential u and v (Figs. 7d and 7e) show that the simulated AP gravity wave is mainly decelerating the flow from the ground to 40 km altitude during the whole 1-d period of simulation. The strongest deceleration occurs in the stratosphere above 15 km, with negative (positive) differential u (v) oscillating between

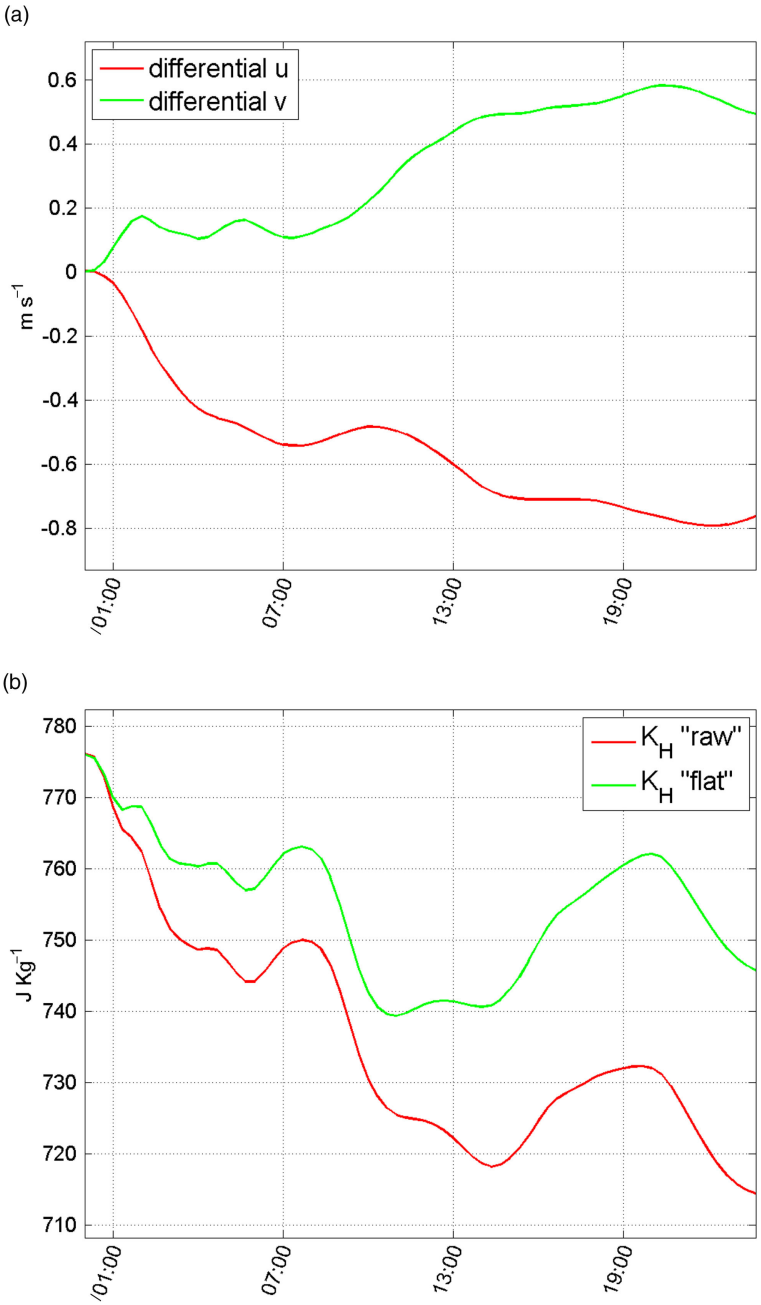

Fig. 8. (a) Time evolution of differential u (red line) and differential v (green line) calculated as a difference between the 20-mininner domain outputs from the WRF simulations, with and without orography, after domain averaging in the inner domain and vertically averaging between 0 and 40 km. The horizontal axis gives the time in hours from 0000 UTC 6 October 2005. The vertical axis gives the intensity in m s^{-1}. (b) As in (a), except for K_H from the WRF experiment, with orography (red line) and without orography (green line) in J kg^{-1}.

0 and -2 ms^{-1} (0 and 2 ms^{-1}), both contributing to a depletion of K_H whose profile in the stratosphere also shows oscillations between 0 and -80 J kg^{-1} (Fig. 7f). Vertically averaging these vertical profiles from the surface to 40 km (Fig. 8a), that is, box-averaging, gives an averaged deceleration of about 0.8 (0.5) ms^{-1} in the u (v) component after 1 d simulation, which corresponds to a decrease of about 4% in terms of kinetic energy (see the 30 J kg^{-1} difference between box-averaged K_H from the simulations with and without the mountain at the end of the simulation in Fig. 8b). Consequently, at the scale of the inner domain used for the domain- and box-averaging

(1500 km × 2580 km), the simulated AP gravity wave does have some decelerating effect on the mean flow. It is then noticeable on Fig. 7d and 7e that there is about a quarter wave period lag between the times the northerly and westerly components reach there maximal deceleration, respectively, which is a typical characteristic of inertial oscillations and therefore supports the analysis of Plougonven et al. (2008). It is then noticeable that these inertial oscillations have a signature in the kinetic energy at the scale of the inner domain, as deduced from the oscillations in the domain-averaged differential K_H (Fig. 7f). These inertial oscillations resemble those obtained by Chen et al. (2007) in their idealised case study of mountain wave, except that in the present case the simulation is extended up to about 45 km (1 hPa) and the inertial oscillations are found one order of magnitude stronger above 15 km altitude, that is, 1 m s^{-1}. The large-scale deceleration triggered by the simulated AP gravity wave and associated secondary inertia-gravity wave generation in the stratosphere are investigated in section 4 with a domain-averaged, then box-averaged, budget analysis of differential u, v and K_H.

3.5. *About the momentum fluxes*

Before analysing the domain-averaged budget of differential u and v in section 4, it is proposed here to compute and discuss the domain-integrated eddy vertical flux of the horizontal momentum components (F_u and F_v) as well as the domain-averaged vertical divergence of F_u and F_v (X_{GW} and Y_{GW}) attributed to the modelled AP gravity wave [cf. eq. (1)]. Indeed Plougonven et al. (2008) computed from their WRF simulation an eddy vertical flux of horizontal momentum in the direction perpendicular to the Antarctic Peninsula ridge ($F_\perp$) that they integrated horizontally over the region 62–65°S, 56–64°W (about 335 km × 380 km), for the period from 0000 to 1800 UTC 7 October. These authors found $F_\perp$ absolute values decreasing with heights, with a magnitude of about 10×10^{10} N at the surface and a local maximum of about 8×10^{10} N at 8–10 km altitude on 7 October morning.

In order to further assess the present simulation with that of Plougonven et al. (2008), $F_\perp$ is compared with F_u and F_v computed as following:

$$(F_u, F_v) = \left[\iint \left((\overline{\rho uw})_{zsraw} - (\overline{\rho uw})_{zsflat} \right) d\alpha d\beta, \iint \left((\overline{\rho vw})_{zsraw} - (\overline{\rho vw})_{zsflat} \right) d\alpha d\beta \right] \quad (5)$$

where α and β stand for the horizontal coordinates [not the terrain-following coordinates x and y in the WRF model used in eq. (2) and eq. (3)], subscripts zsraw and zsflat specify the quantities taken from the simulation with and without orography, respectively, and — stands for the domain averaging in the inner domain of size 1500 km × 2580 km. The time–height profiles of F_u and F_v are displayed in Fig. 9a and 9b for the simulated period from 0000 UTC 6 October to 0000 UTC 7 October. It shows enhanced values of order ± 10–20×10^{10} N in the troposphere–lower stratosphere, decreasing with height.

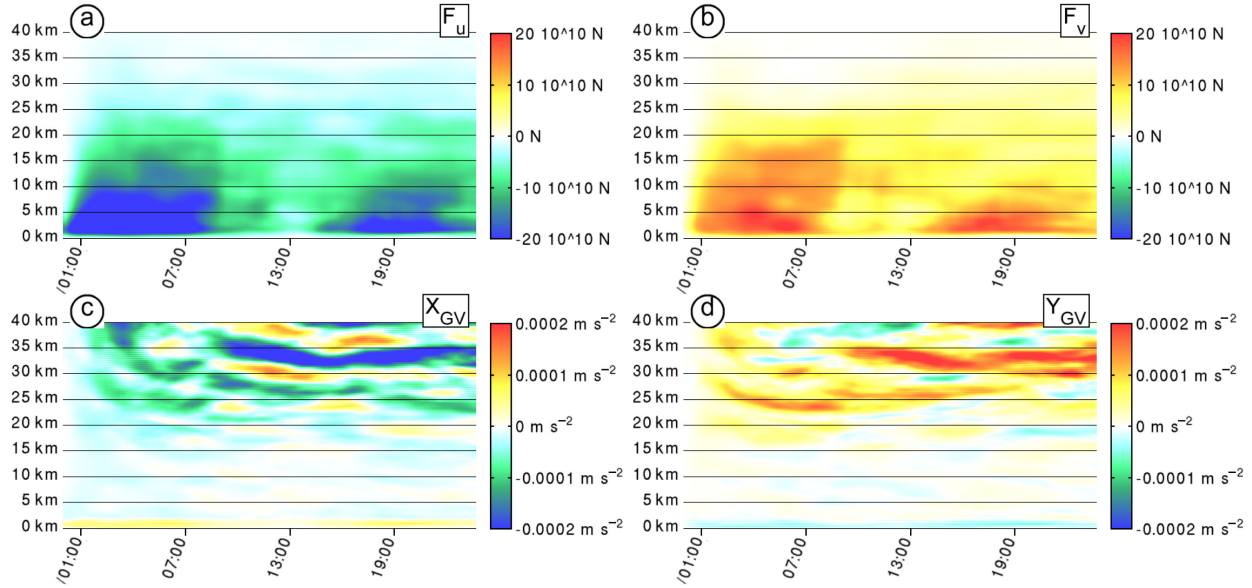

Fig. 9. (a) As in Fig. 7a, except for F_u. (b) As in (a), except for F_v. (c) As in (a), except for X_{GW}. (d) As in (a), except for Y_{GW}.

This is rather comparable to what was found by Plougonven et al. (2008), taking into account that the results displayed here are from 0000 UTC 6 October to 0000 UTC 7 October, and not from 0000 to 1800 UTC 7 October, and that the domain used for the integration here is much bigger (compare the 1500 km × 2580 km domain's size used here to the 335 km × 380 km domain's size used in Plougonven et al., 2008).

However, it is has to be noted here that it is the vertical divergence of F_u and F_v, namely X_{GW} and Y_{GW} in eq. (1), that forces the mean flow. In order to link the results of Plougonven et al. (2008) with the domain-averaged budget analysis of differential u and v in section 4, it is proposed here to compute the domain-averaged X_{GW} and Y_{GW} as following:

$$(X_{GW}, Y_{GW}) = \left[-\left(\left(\frac{1}{\overline{\rho}} \frac{\partial}{\partial z} (\overline{\rho u w}) \right)_{zsraw} - \left(\frac{1}{\overline{\rho}} \frac{\partial}{\partial z} (\overline{\rho u w}) \right)_{zsflat} \right), - \left(\left(\frac{1}{\overline{\rho}} \frac{\partial}{\partial z} (\overline{\rho v w}) \right)_{zsraw} - \left(\frac{1}{\overline{\rho}} \frac{\partial}{\partial z} (\overline{\rho v w}) \right)_{zsflat} \right) \right] \quad (6)$$

where all of the symbols have already been defined above. The domain-averaged X_{GW} and Y_{GW} are displayed in Fig. 9c and 9d, respectively. Taking into account the fact that the domain-averaged u (v) component is positive (negative) from the surface to 40 km altitude (cf. Fig. 7a and 7b), the red/positive (blue/negative) shades in Fig. 9c (9d) below 2 km mean that the domain-averaged X_{GW} and Y_{GW} have an accelerating effect in the lowest levels. It is then noticeable that the domain-averaged X_{GW} and Y_{GW} mainly have a decelerating effect above 2 km altitude, mainly above 15 km altitude, as deduced from the mainly blue/negative (red/positive) shades in Fig. 9c (9d) at these heights (confirming Plougonven et al., 2008). These results are further discussed in the following section.

4. Quantitative analysis of the gravity wave forcing on the mean flow

4.1. Method

4.1.1 Budget of horizontal wind components. Following Durran and Klemp (1995) and Héreil and Stein (1999) who quantified gravity wave forcing on the mean flow with a budget of momentum in two-dimensional case studies, it is proposed here to conduct a similar budget analysis for the simulated AP gravity wave based on the equations of motion solved in the WRF model, that is, eq. (2) and eq. (3). Developing the expression of the contravariant component Ω (eq. 4) in the total divergence of U/V flux terms (2b/3b) allows separation of the horizontal and vertical divergence of U/V fluxes:

$$\underbrace{-\frac{1}{\mu}\left[(Uu)_x+(Vu)_y+(\Omega u)_\eta\right]}_{\text{7a:Budgetu\_divfluxt}} = \underbrace{-\frac{1}{\mu}\left[(Uu)_x-\left(\frac{\Phi_x}{\Phi_\eta}Uu\right)_\eta+(Vu)_y-\left(\frac{\Phi_y}{\Phi_\eta}Vu\right)_\eta\right]}_{\text{7b:Budgetu\_divfluxh}} \underbrace{-\frac{1}{\mu}\left[\left(\frac{g}{\Phi_\eta}Wu\right)_\eta\right]}_{\text{7c:Budgetu\_divfluxv}} \quad (7)$$

$$\underbrace{-\frac{1}{\mu}\left[(Uv)_x+(Vv)_y+(\Omega v)_\eta\right]}_{\text{8a:Budgetv\_divfluxt}} = \underbrace{-\frac{1}{\mu}\left[(Uv)_x-\left(\frac{\Phi_x}{\Phi_\eta}Uv\right)_\eta+(Vv)_y-\left(\frac{\Phi_y}{\Phi_\eta}Vv\right)_\eta\right]}_{\text{8b:Budgetv\_divfluxh}} \underbrace{-\frac{1}{\mu}\left[\left(\frac{g}{\Phi_\eta}Wv\right)_\eta\right]}_{\text{8c:Budgetv\_divfluxv}} \quad (8)$$

where the total divergence of U/V fluxes (7a/8a) is the sum of the horizontal divergence of horizontal fluxes of U/V (7b/8b) and the vertical divergence of vertical fluxes of U/V (7c/8c).

Terms of eq. (2) and eq. (3), including terms of eq. (7) and eq. (8), are then integrated each time step during the simulation and are saved in the inner domain's output files every 20 min as 3D fields. It is then possible to average these terms in any box for any time-period multiple of 20 min, in order to make a so-called box-averaged budget analysis. Averaging these equations in a horizontal domain, (2a/2a) gives the time evolution of u and v for the flow inside the domain, that is, the inner flow, (7b/8b) gives the amount of U and V exchanged horizontally between the inner and outer flow, that is, the flow outside the considered domain, (7c/8c) gives the amount of U and V transported vertically in the inner flow by large- and fine scale processes, gravity waves being one of them, (2c/3c) and (2d/3d) give the state of geostrophic balance between the pressure and Coriolis forces for the inner flow, and (2e/3e) gives the amount of u and v dissipated by frictional processes in the inner flow, mainly in the boundary layer. To simplify the discussion in the next sections, (7b/8b) and (7c/8c) will be referred to as horizontal and vertical divergence of momentum flux, respectively. Because eq. (7) and eq. (8) are not strictly verified in the numerical model, the obtained budget is not exactly equilibrated at grid points, which is why the tendency is systematically compared to the sum of the source terms when discussing the results.

4.1.2 Budget of horizontal kinetic energy. As noticed by Arnault and Kirkwood (2012), the sign of a decelerating term in the budget of zonal/meridional wind is either negative (positive) for the deceleration of westerlies/southerlies (easterlies/northerlies). Whereas, the interpretation of the sign of the terms in the budget of horizontal kinetic energy $KH = 0.5*(u^2+v^2)$ is more straightforward since a decelerating (accelerating) term is necessarily negative (positive) in this case. It is therefore argued that the budget of KH is more convenient to diagnose the impact of gravity waves on the horizontal flow.

Reformulating eq. (2) and eq. (3) in their advective form, including the developed expression of the contravariant component Ω of eq. (4), Arnault and Kirkwood (2012) obtained:

$$\begin{aligned}
&\underbrace{u_t}_{\text{9a:Budgetu_tend}} = \underbrace{-u\left(u_x-\frac{\Phi_x}{\Phi_\eta}u_\eta\right)-v\left(u_y-\frac{\Phi_y}{\Phi_\eta}u_\eta\right)}_{\text{9b:Budgetu_advh}} \\
&\underbrace{-w\frac{g}{\Phi_\eta}u_\eta}_{\text{9c:Budgetu_advv}} \underbrace{-\alpha\left(p_x-\frac{\Phi_x}{\Phi_\eta}p_\eta\right)}_{\text{9d:Budgetu_pres}} \underbrace{+f\cdot v}_{\text{9e:Budgetu_cori}} \underbrace{+F_x}_{\text{9f:Budgetu_fric}}
\end{aligned} \tag{9}$$

$$\begin{aligned}
&\underbrace{v_t}_{\text{10a:Budgetv_tend}} = \underbrace{-u\left(v_x-\frac{\Phi_x}{\Phi_\eta}v_\eta\right)-v\left(v_y-\frac{\Phi_y}{\Phi_\eta}v_\eta\right)}_{\text{10b:Budgetv_advh}} \\
&\underbrace{-w\frac{g}{\Phi_\eta}v_\eta}_{\text{10c:Budgetv_advv}} \underbrace{-\alpha\left(p_y-\frac{\Phi_x}{\Phi_\eta}p_\eta\right)}_{\text{10d:Budgetu_pres}} \underbrace{-f\cdot u}_{\text{10e:Budgetu_cori}} \underbrace{+F_v}_{\text{10f:Budgetv_fric}}
\end{aligned} \tag{10}$$

above two orders of magnitude, eq. (9), eq. (10), eq. (2) and eq. (3) are considered here as the same equations with a different formulation, so that the total divergence of U and V normalised by μ is equal to the total advection of u and v, respectively. This result is coherent with the fact that these equations are written in a mass-coordinate system, that is, comparable to a typical pressure coordinate system but without the assumption of hydrostatic balance (Klemp et al., 2007). However, the horizontal (vertical) divergence of U/V flux normalised by μ is not necessarily equal to the horizontal (vertical) advection of u/v. Nevertheless Arnault and Kirkwood (2012) multiplied eq. (9) and eq. (10) by u and v, respectively, in order to obtain an equation of K_H in its advective form.

Since an equation in its flux form is more suited to discuss the exchanges between the inner and outer flow in a box-averaged budget, it is proposed here to derive an equation of K_H in its flux form. Remarking that:

$$\frac{1}{\mu}\left(\mu u\frac{u^2}{2}\right)_x = \frac{u}{2}\left(uu_x+\frac{1}{\mu}(\mu uu)_x\right)$$

and applying this property to u and v for the three coordinates x, y and η gives the following prognostic equation of K_H in its flux form:

$$\begin{aligned}
&\underbrace{uu_t+vv_t}_{\text{11a:BudgetK}_H\text{_tend}} = \underbrace{+\frac{u}{2}\cdot(\text{Budgetu_advh}+\text{Budgetu_divfluxh})+\frac{v}{2}\cdot(\text{Budgetv_advh}+\text{Budgetv_divfluxh})}_{\text{11b:BudgetK}_H\text{_divfluxh}} \\
&\underbrace{+\frac{u}{2}\cdot(\text{Budgetu_advv}+\text{Budgetu_divfluxv})+\frac{v}{2}\cdot(\text{Budgetv_advv}+\text{Budgetv_divfluxv})}_{\text{11c:BudgetK}_H\text{_divfluxv}} \\
&+\underbrace{u\cdot\text{Budgetu_pres}+v\cdot\text{Budgetv_pres}}_{\text{11d:BudgetK}_H\text{_pres}}+\underbrace{u\cdot\text{BudgetVu_fric}+v\cdot\text{Budgetv_fric}}_{\text{11e:BudgetK}_H\text{_fric}}
\end{aligned} \tag{11}$$

where (9b/10b) and (9c/10c) are the horizontal and vertical advections of u/v, respectively, and the other terms were already defined in eq. (2) and eq. (3). Since it has been found in the present case that after box-averaging, $U_t/\mu = u_t$ and $V_t/\mu = v_t$ with an accuracy where the quantities Budgetu_..., Budgetv_... are already defined in eq. (2), eq. (3), eq. (5), eq. (8), eq. (9) and eq. (10). Averaging eq. (11) in a horizontal domain, (11a) gives the time evolution of K_H of the inner flow, (11b) gives the amount of K_H exchanged horizontally between the inner

and outer flow, (11c) gives the amount of K_H transported vertically by the inner flow, (11d) gives the energetic impact of the ageostrophic circulation on inner flow and (11e) gives the amount of K_H dissipated by frictional processes in the inner flow. The physical interpretation of the terms in the budget of K_H is actually similar to those in the budgets of u and v except that the effect of the Coriolis force does not appear explicitly in eq. (11), since this force does not work, but indirectly in the pressure work through geostrophic imbalance. Moreover this pressure work can also be interpreted as a local formulation for the so-called baroclinic conversion between the potential energy of the atmosphere and the horizontal kinetic energy, as it was originally proposed by Lorenz (1955) for studying the energetics of the general circulation and applied locally by Arnault and Roux (2009), among others, for studying the energetics of a developing African easterly wave in a finite domain. It is interesting to note for the physical interpretation of this baroclinic conversion term that it can only result from the ageostrophic component of the wind.

As for the budgets of u and v, the budget of K_H presented here is not exactly equilibrated at grid points, so the tendency will also be compared to the sum of the source terms when discussing the results. Finally, in order to separate the contribution of mountain waves from that of other synoptic processes of non-orographic origin in the domain- and box-averaged budget analysis, each of the terms of the budgets is computed as the difference between the results of the simulations with and without orography (as in Arnault and Kirkwood, 2012).

4.2. Results for the budget of horizontal wind components

4.2.1. Domain-averaged results. The physical processes responsible for the temporal variations of the domain-averaged differential u and v discussed in section 3.4 (Fig. 7d and 7e) are investigated here with the temporal variations of the domain-averaged terms of the prognostic eq. (2) and eq. (3), including eq. (7) and eq. (8), applied to differential u and v (Figs. 10 and 11). It is noteworthy that the domain-averaged budgets of differential u and v are much better equilibrated (compare Fig. 10a, 10b and 10j; Fig. 11a, 11b and 11j) compared to what was obtained by Arnault and Kirkwood (2012) in their domain-averaged budget of differential KH, mainly because the dynamical influence of this AP gravity wave is much stronger so the tendency terms have an order of magnitude comparable to that of the source terms (not one order below as in Arnault and Kirkwood, 2012).

It is also noteworthy that the domain-averaged differential vertical-divergence of momentum flux terms (Figs. 10h and 11h) computed in the mass-coordinate framework (terms 7c, 8c of eq. (7) and eq. (8), respectively) are rather comparable to the domain-averaged X_{GW} and Y_{GW} (Fig. 9c and 9d) computed in the height coordinate framework [eq. (6)]. Since WRF resolves the non-hydrostatic compressible equations using terrain-following mass coordinates, the computation of X_{GW} and Y_{GW} requires interpolations, thus explaining the differences between Fig. 9c and 9d and Figs. 10h and 11h, respectively.

In the lowest levels, below 2 km altitude, the differential, that is, wave induced, pressure force has a decelerating effect both on the u and v component (cf blue/negative shades in Fig. 10g, red/positive shades in Fig. 11g, below 2 km), keeping in mind that domain-averaged u (v) is positive (negative) (Fig. 7d and 7e). This low-level decelerating pressure force is then partly counterbalanced by an accelerating total divergence of momentum flux (cf. red/positive shades in Fig. 10d, blue/negative shades in Fig. 11d, below 2 km), this last one being separated in a stronger accelerating vertical divergence of momentum flux (cf. red/positive shades in Fig. 10h, blue/negative shades in 11 h, below 2 km) and smaller decelerating horizontal divergence of momentum flux (cf. blue/negative shades in Fig. 10f, red/positive shades in Fig. 11f, below 2 km). Above 2 km the vertical divergence of momentum flux mainly decelerates the flow, especially above 15 km (cf. blue/negative shades in Fig. 10f, red/positive shades in Fig. 11f, above 2 km), this effect being partly counterbalanced by a weaker accelerating horizontal divergence of momentum flux above 2 km (compare Fig. 10d, 10f and 10h; then Fig. 11d, 11f and 11h).

The above analysis supports the interpretation of Durran and Klemp (1995) and Héreil and Stein (1999) according to whom the topography has a direct decelerating effect on the mean flow through a pressure drag in the lowest levels, while gravity waves counterbalance this low-level sink, at least partially, by extracting and transporting downward horizontal momentum from the flow aloft, in this particular case mainly from above 15 km altitude. Moreover in this case the downward transport of momentum is also associated with a supply of momentum from the outer flow through accelerating horizontal divergence of momentum flux above 2 km. This suggests that the simulated AP gravity wave has some dynamical influence on scales larger than that of the inner domain used for the domain-averaged budget, that is, 1500 km $\times$ 2580 km, thus confirming the remote effect of gravity wave forcing proposed by Durran and Klemp (1995) and Héreil and Stein (1999).

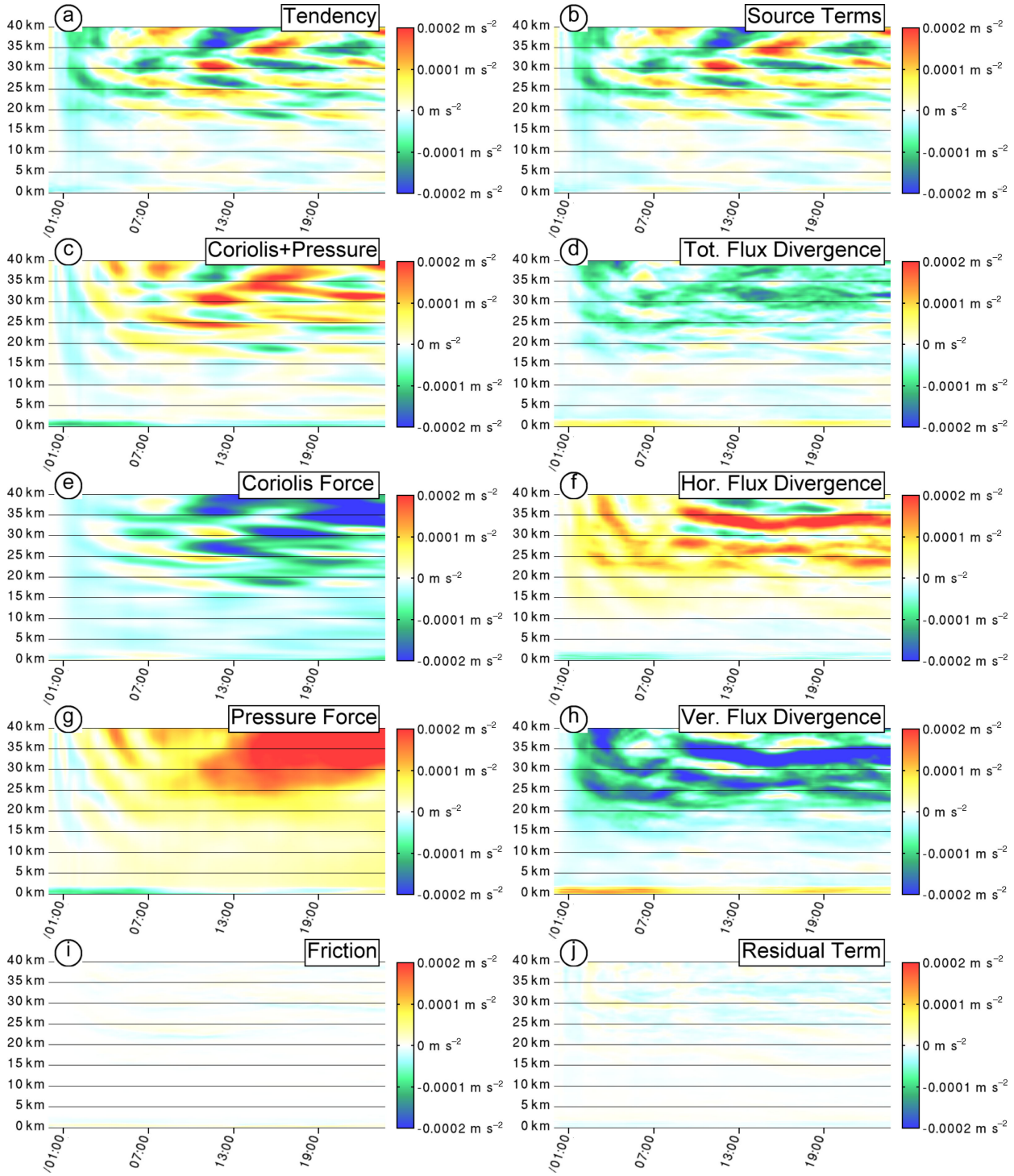

Fig. 10. As in Fig. 7, except for the difference of the terms of the budget of u in m s^{-2}: (a) tendency, (b) sum of the source terms, (c) sum of the Coriolis and pressure forces, (d) total-flux divergence, (e) Coriolis force, (f) horizontal flux divergence, (g) pressure force, (h) vertical flux divergence, (i) friction and (j) residual term.

This budget analysis further shows that the decelerating effect in the stratosphere triggered by the vertical divergence of momentum flux is mainly counterbalanced by a negative (positive) Coriolis (pressure force) having a decelerating and accelerating (accelerating and decelerating) effect in the budgets of u and v, respectively

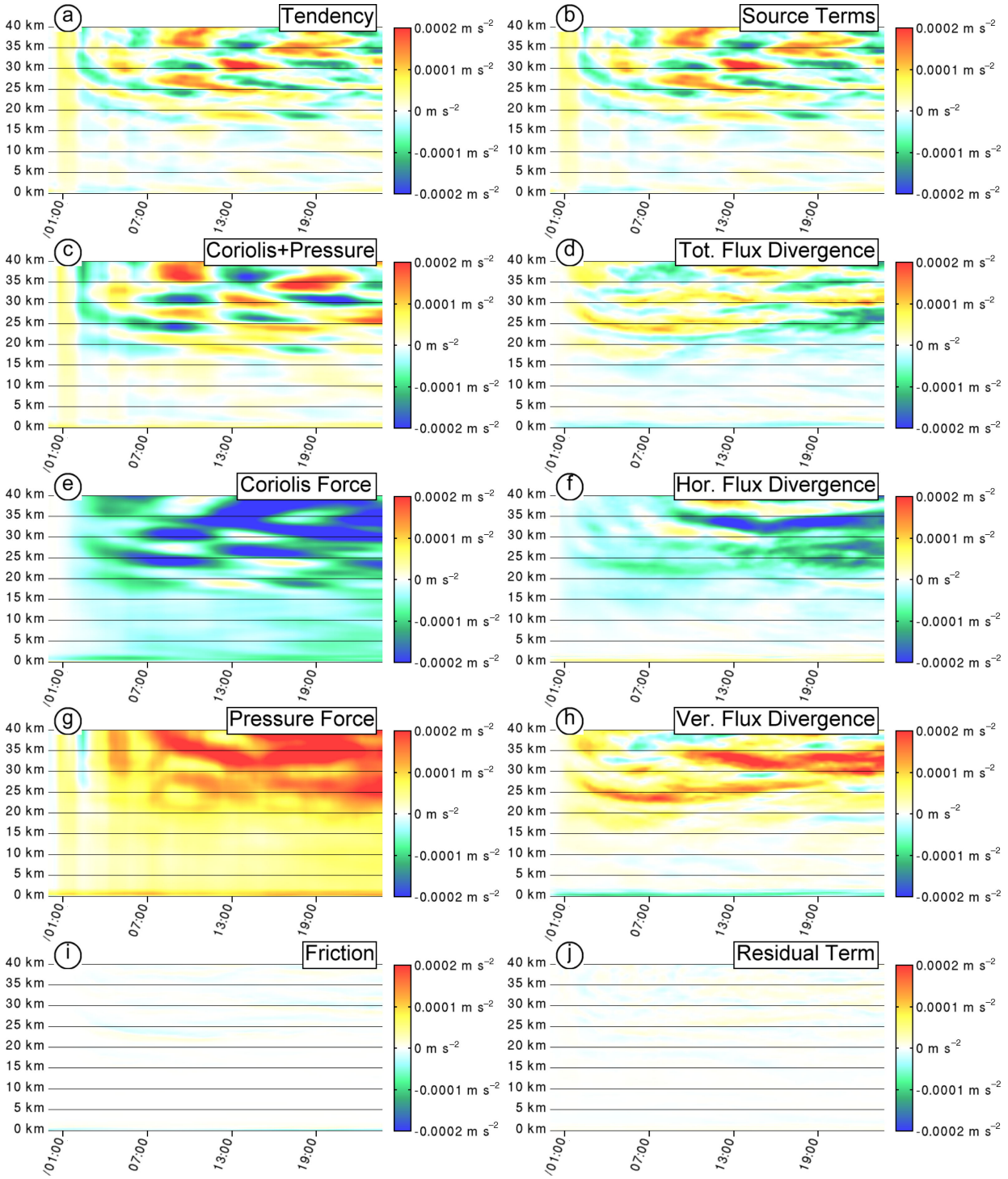

Fig. 11. As in Fig. 10, except for the budget of differential v.

(cf. blue/negative shades in Figs. 10e and 11e; red/positive shades in Figs. 10g and 11g, above 2 km). Indeed at the scale of the budget presented here, that is, 1500 km × 2580 km, adjusting processes due to earth rotation, that is, geostrophic adjustment, certainly play a significant role in the dynamical influence of the simulated AP gravity wave. It has to be noticed here that frictional dissipation has a negligible impact in these budgets (Figs. 10i and 11i).

The resulting tendencies of domain-averaged differential u and v (Figs. 10a and 11b) then show the oscillations associated with the secondary inertia-gravity wave generated in the stratosphere (cf. Fig. 7d and 7e; Plougonven et al., 2008). Therefore, according to this budget analysis, this secondary inertia-gravity wave is mainly triggered by a geostrophic imbalance between the Coriolis and pressure forces, although some non-linear, that is, non-conservative, dynamics is also at stake as deduced from the contribution of the domain-averaged differential total flux divergence term (compare Fig. 10a, 10c and 10d; Fig. 11a, 11c and 11d).

These results can be interpreted as following. The simulated AP gravity wave is breaking in the stratosphere, in association with a wave-induced decelerating vertical flux divergence of momentum. This creates a geostrophic imbalance that consequently generates an inertia-gravity wave, thus supporting the cause-consequence relationship between gravity wave breaking, momentum deposition and secondary inertia-gravity wave generation (e.g. Scavuzzo et al., 1998; Vadas et al., 2003; Plougonven et al., 2008; Spiga et al., 2008). The 1500 km $\times$ 2580 km-scale dynamical impact then results from the interaction between this wave-induced decelerating vertical divergence of momentum flux, geostrophic adjustment dynamics involving the secondary inertia-gravity wave and momentum exchange with the larger scale through accelerating horizontal divergence of momentum flux.

4.2.2. Box-averaged results. In order to quantify the impact of the AP gravity wave on the whole simulated atmosphere within the inner domain, the vertical profiles of Figs. 10 and 11 are averaged vertically between 0 and 40 km to obtain the so-called box-averaged budgets of Fig. 12. Figure 12a and 12c shows a transition period during the first three hours of the simulation when the horizontal and vertical divergence of momentum flux increase from zero to about ± 3–5×10^{-4} ms^{-2} (green solid lines with circles and plus signs in Fig. 12a and 12c, respectively), with the pressure force having a dominant effect during the first hour (compare tendency, that is, blue solid lines, and pressure force, that is, red solid line with circles, in Fig. 12a and 12c). Consequently, the deceleration of u and v during this transition period is about two times stronger than during the rest of the simulation (especially true for the u-component, see blue curves in Fig. 12a and 12c), which is coherent with the fact that the AP gravity wave structure provided by the ECMWF analyses at the initial time of the simulation has to adjust to the finer resolution used for the WRF model experiment discussed here. Nevertheless, it is assumed that the whole simulation is realistic enough so that analysing the physical processes resolved in the model help understanding the physical processes occurring in the real atmosphere.

These box-averaged budgets show that the decelerating vertical divergence of momentum flux is partly counterbalanced by an accelerating horizontal divergence of momentum flux (compare green lines with plus signs and circles in Fig. 12a and 12c), as already deduced from the vertical profiles of Figs. 10 and 11. These box-averaged budgets also show a constantly decreasing Coriolis force (red solid line with plus signs in Fig. 12a and 12c) due to an averaged decelerating effect (Fig. 8a) (and a negative Coriolis parameter in the Southern hemisphere), overcompensated by the pressure force (red solid line with circles in Fig. 12a and 12c). The resulting box-averaged tendencies of differential u and v then display the signature of the secondary inertia–gravity wave developing in the stratosphere discussed above (e.g. Fig. 7d and 7e).

These results suggest that at the scale of the inner domain, that is, 1500 km $\times$ 2580 km, one part of the vertical transport of momentum triggered by the simulated AP gravity wave induces a geostrophically balanced deceleration of the flow between 0 and 40 km, another part generates an ageostrophic circulation, that is, the secondary inertia–gravity wave, a third part triggers a momentum transfer with the larger scales at the lateral boundaries of the box and a last part results in a momentum transfer with the atmosphere above 40 km, which is consistent with the expectation that gravity waves significantly influence the large-scale dynamics of the middle atmosphere (e.g. Fritts and Alexander, 2003).

A comparison between the tendency, the total divergence of momentum flux and the sum of the Coriolis and pressure forces in Fig. 12b and 12d summarises these results. In particular, in a box of horizontal size 1500 km $\times$ 2580 km extending vertically from 0 to 40 km, the simulated AP gravity wave disturbs the geostrophic balance of the inner flow and triggers momentum exchanges with the outer flow both at the lateral and upper boundaries, resulting in a global deceleration of the inner flow as well as in the generation of a secondary inertia–gravity wave. This aspect is further investigated in the following section with a budget of horizontal kinetic energy.

4.3. *Results for the budget of horizontal kinetic energy*

4.3.1. Domain-averaged results. As for the domain-averaged budgets of differential u and v, the domain-averaged budget of differential KH is fairly well equilibrated (compare Fig. 13a, 13b and 13g). It is then interesting to see that the pressure drag discussed in section 4.2.1 has a small impact on the pressure work (see blue shades in Fig. 13c, below 2 km), which means that the

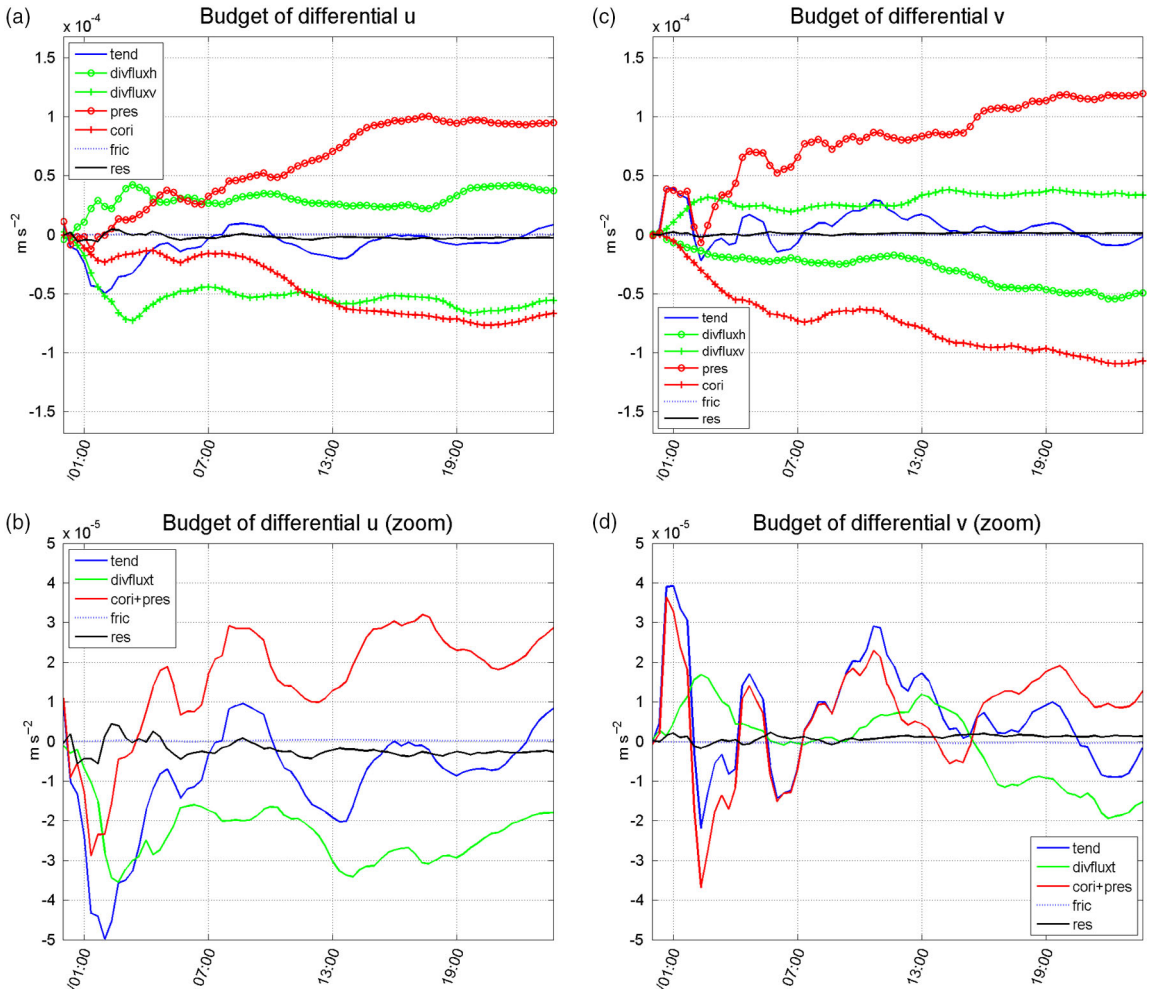

Fig. 12. (a) As in Fig. 8a, except for the terms of the budget of differential u in m s^{-2}. The coefficients displayed are the tendency (solid blue line); the horizontal flux divergence (solid green line with circles), the vertical flux divergence (solid green line with plus signs), the pressure force (solid red line with circles), the Coriolis force (solid red line with plus signs), the frictional force (dashed dark line) and the residual term (solid dark line). (b) As in (a), except that the sum of horizontal and vertical flux divergence, that is, total-flux divergence (green line) and the sum of Coriolis and pressure forces (red line) are represented instead. (c) As in (a), except for the budget of differential v. (d) As in (b), except for the budget of differential v.

direct decelerating effect of topography on the mean flow corresponds to a negative baroclinic conversion, that is, kinetic energy converted into potential energy. This low-level negative baroclinic conversion is then completely balanced by a stronger positive (smaller negative) vertical (horizontal) divergence of KH flux (compare Fig. 13a, 13c, 13f and 13h, below 2 km).

Similarly to what was obtained for the domain-averaged budgets of differential u and v above 2 km (cf. section 4.2.1), the vertical divergence of K_H flux is also mainly negative above 2 km, especially above 15 km (Fig. 13h), this effect being partly counterbalanced by a weaker and mainly positive horizontal divergence of K_H flux above 2 km (compare Fig. 13d, 13f and 13h, above 2 km). A comparison with the tendency of differential K_H (Fig. 13a) then shows that the decelerating effect in the stratosphere triggered by vertical divergence of K_H flux is mainly counterbalanced by a positive pressure work, that is, positive baroclinic conversion (compare Fig. 13a, 13c and 13d), the sum of these source terms resulting in oscillations characterising the secondary inertia–gravity wave discussed above.

These results are very similar to those obtained from the domain-averaged budgets of u and v in section 4.2.1, except that frictional dissipation associated with enhanced turbulence in the convectively overturning regions in the stratosphere (cf. Figs. 5d, 5e, 6d and 6e) has a stronger impact in the budget of energy compared to that of u and v (compare Figs. 10i, 11i and 13e). Subsequently, the energetic point of view allows further interpretation of

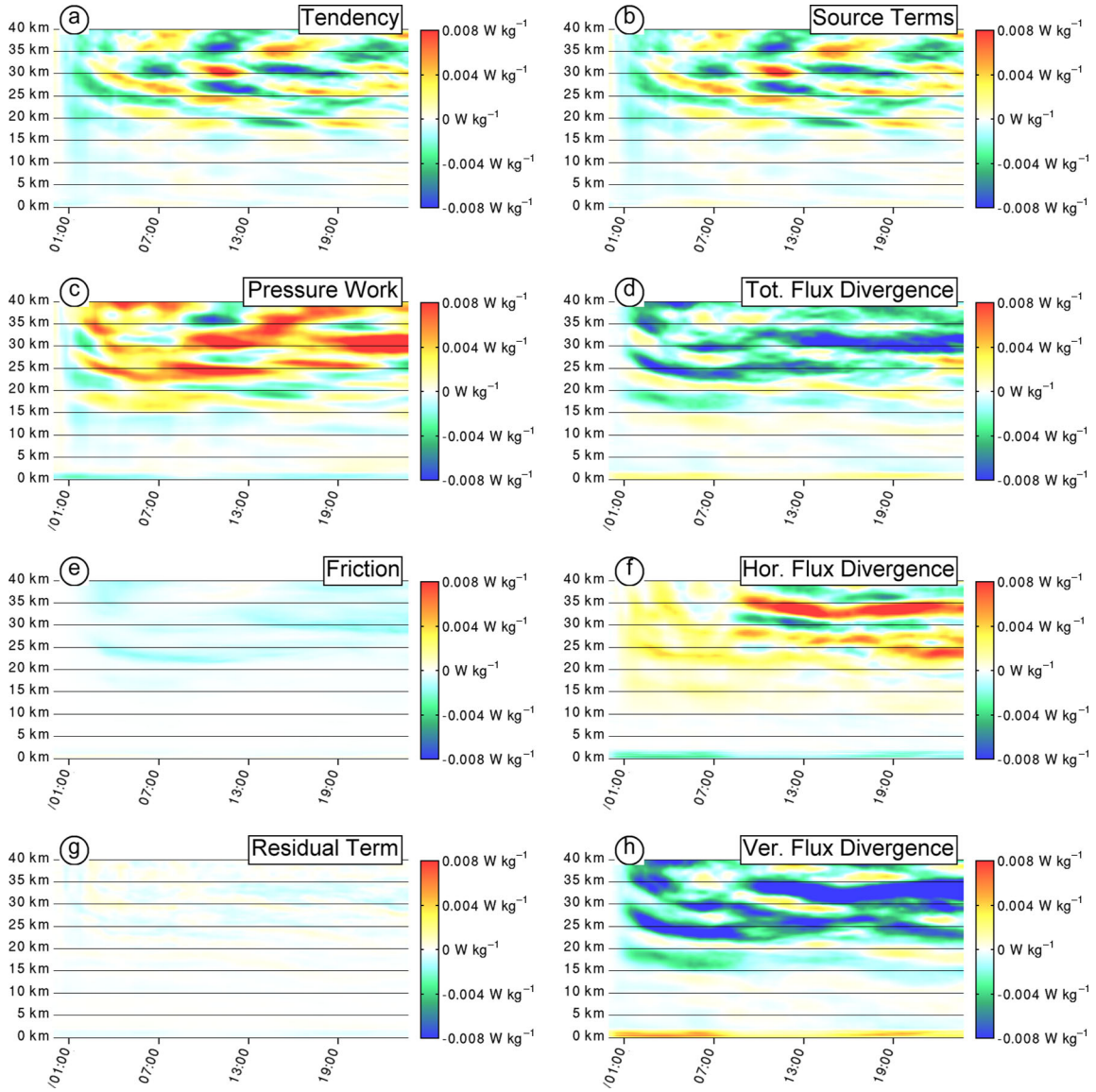

Fig. 13. As in Fig. 10, except for the differential budget of K_H. (a) tendency, (b) sum of the source terms, (c) pressure work, (d) total-flux divergence, (e) friction, (f) horizontal flux divergence, (g) residual term and (h) vertical flux divergence.

the simulated physical processes. In particular the extraction and downward transport of kinetic energy from the flow above 15 km inside the 1500 km × 2580 km inner domain is associated with a supply of kinetic energy from the outer flow through positive horizontal divergence of K_H flux, as well as a supply of kinetic energy from the potential energy through a positive baroclinic conversion. Since this baroclinic conversion, that is, pressure work, is done by the ageostrophic circulation, it is argued here that this kinetic energy supply from the potential energy is the effect of the secondary inertia–gravity wave, that is, the ageostrophic circulation in the inner domain according to the above discussion (cf. sections 4.2.1 and 4.2.2).

4.3.2. Box-averaged result. As for the budgets of differential u and v, the box-averaged budget of differential KH is also shown here (Fig. 14). As previously discussed, a transition period of about three hours is also clearly seen in Fig. 14, with a tendency term (blue solid line in Fig. 14) following the quick decrease of the pressure work (red solid line in Fig. 14) during the first hour, then the decrease of vertical divergence of KH flux (green solid line with plus signs in Fig. 14) for the next two hours. There is also a sharp increase of turbulent dissipation after the second hour (blue dashed line), due to the fact that in the model the AP gravity wave starts to break and enhance turbulence in localised stratospheric regions from that time.

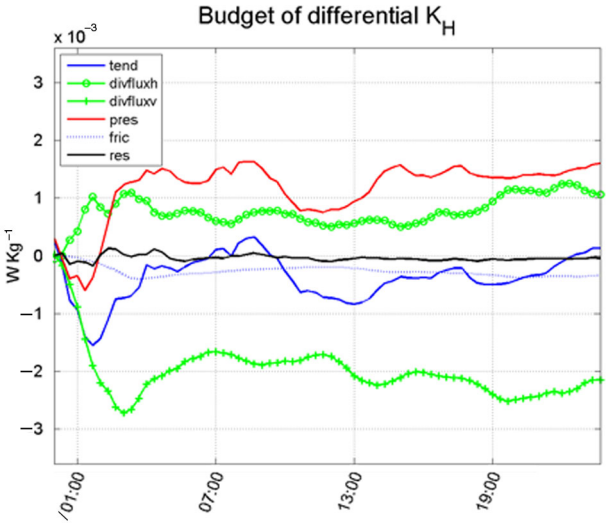

Fig. 14. As in Fig. 8a, except for the terms of the budget of differential KH in W kg^{-1}. The coefficients displayed are the tendency (solid blue line), the horizontal flux divergence (solid green line with circles), the vertical flux divergence (solid green line with plus signs), the pressure work (solid red line), the frictional dissipation (dashed dark line) and the residual term (solid dark line).

This transition phase may therefore have enhanced unrealistically the deceleration of the flow in the beginning of the simulation as already discussed in section 4.2.2.

Figure 14 mainly shows that after averaging horizontally in the 1500 km $\times$ 2580 km-inner domain and vertically between 0 and 40 km, the decrease of differential K_H (blue solid line in Fig. 14), the turbulent dissipation (blue dashed line) and the transfer of kinetic energy to the atmosphere above 40 km (green solid line with plus signs in Fig. 14) are balanced by a strong supply of kinetic energy from the potential energy of the inner flow (red solid line in Fig. 14) and a two times smaller supply of kinetic energy from the outer flow at the lateral boundaries (green solid line with circles in Fig. 14).

5. Conclusion

Based on balloon measurement, radiosounding, ECMWF analyses and a WRF model experiment, Plougonven et al. (2008) suggested that a gravity wave induced by the Antarctic Peninsula on 6–7 October 2005 was breaking in the stratosphere, in association with deposition of momentum in the opposite direction of the mean flow and generation of a secondary inertia–gravity wave. This real-case study has been revisited here in order to quantify the dynamical influence of this so-called AP gravity wave with a box-averaged budget analysis of u and v adapted from the two-dimensional case studies of Durran and Klemp (1995) and Héreil and Stein (1999). The budget of K_H has also been considered in order to complement the analysis of the physical processes at stake.

The WRF modelling experiment conducted in this work was similar to that of Plougonven et al. (2008), with in particular a 6 km horizontal resolution for the inner domain and 153 vertical levels with a model top at 1 hPa, except that in this case the inner domain was roughly six times larger, that is, 1500 km $\times$ 2580 km, allowing better resolution of the large-scale dynamics associated with the secondary inertia–gravity wave. The outer domain for the present WRF simulation was then chosen relatively large, that is, 3600 km $\times$ 9000 km, and coupled with the inner domain using a two-way grid-nesting technique, in order to resolve the large-scale circulation eventually modified by the AP gravity wave dynamics resolved in the inner domain. It was thus possible to study the dynamical impact of the simulated AP gravity wave within the whole inner domain without having spurious counterbalancing pressure and momentum flux gradients due to fixed lateral boundary conditions (Héreil and Stein, 1999).

The model results were very similar to those of Plougonven et al. (2008), with in particular a gravity wave characterised by an intrinsic period of 14–34 min, vertical velocity oscillations of order of magnitude $+/-2$ m s^{-1} up to 40 km altitude, horizontal wind oscillations of order of magnitude $+/-15$–25 ms^{-1}, a horizontal wavelength of about 30–60 km slightly increasing with height, a vertical wavelength of about 8 km in the troposphere, reduced to about 5 km in the stratosphere, regions of convective overturning in the stratosphere associated with enhanced turbulence and generation of a secondary inertia–gravity wave. It was then shown that these convective overturning regions were associated with shedding streamwise counter vortices that eventually played a role in the large-scale dynamical influence of the simulated AP gravity wave (e.g. Fritts et al., 1999; Chen et al., 2007).

In order to quantify the dynamical impact of this simulated AP gravity wave, the results of this WRF experiment were compared to a control simulation with flat orography. The two numerical experiments, with and without orography, were then conducted for a 1-d period, from 0000 UTC 6 October 2005, after which the two model results already showed quantitative differences. In particular, after averaging horizontally in the entire inner domain, that is, domain averaging, and vertically from 0 to 40 km, that is, box-averaging, and comparing with the results from the simulation without orography, it was shown that after 1 d of simulation the modelled AP gravity wave was associated with a box-averaged deceleration of about 0.8 (0.5) ms^{-1} in the u (v) component, corresponding to a decrease of about 4% in terms of kinetic energy (Fig. 8).

The eddy vertical flux of horizontal momentum was then evaluated as a difference between the simulations with and without orography and integrated horizontally on the inner domain. The results showed enhanced values of order ± 10–20×10^{10} N in the troposphere – lower stratosphere, decreasing with height, which is about two times bigger but still comparable to what was obtained by Plougonven et al. (2008), recalling the fact that they used a much smaller, that is, 335 km $\times$ 380 km, domain for the horizontal integration and visualised the results on 7 October, not on 6 October as here. The domain-averaged eddy vertical flux of horizontal momentum was then vertically derived using the height coordinate and divided by the domain-averaged density in order to evaluate the momentum forcing of eq. (1). This term did confirm the decelerating effect of the AP gravity wave in the stratosphere suggested by Plougonven et al. (2008), and further appeared to be rather similar to its equivalent in the mass-coordinate system used in the WRF model (terms 7c and 8c in eq. (7) and eq. (8)) (compare Figs. 9c, 9d, 10h and 11h), thus justifying the method of deriving the budgets of u, v and K_H in the mass-coordinate system of the WRF model.

Indeed the WRF model resolves the equations of motion on a terrain-following mass-coordinate system (Klemp et al., 2007; Skamarock and Klemp, 2008), so it was possible to derive budgets of u and v using flux-form equations, at least in the WRF experiments conducted in the present work. More particularly in the proposed (domain-, box) averaged budget analysis of u and v, the tendency of averaged u/v was compared to the sum of averaged horizontal and vertical divergence of U/V fluxes, averaged pressure, Coriolis and frictional forces, where U and V are the horizontal components of the momentum form used in the WRF model, that is, u/v times the vertically integrated mass μ. The divergence of U/V fluxes was consequently interpreted as a divergence of momentum flux. A budget of $K_H = 0.5*(u^2+v^2)$ using a flux-form equation could then be derived from the above budgets of u and v. More particularly in the proposed domain- and box-averaged budget analysis of K_H, the tendency of averaged K_H was compared to the sum of averaged horizontal and vertical divergence of K_H flux, averaged pressure work and frictional dissipation. Following Lorenz (1955) and Arnault and Roux (2009), the pressure work was then interpreted as the local formulation of the so-called baroclinic conversion between the potential energy of the atmosphere and K_H, keeping in mind that this pressure work actually results from the ageostrophic component of the wind.

Because the present article aims at quantifying the dynamical influence of the simulated AP gravity wave on the large-scale circulation, that is, large-scale winds, it was claimed that analysing the budgets of u, v and K_H was certainly well adapted for that purpose. Following Arnault and Kirkwood (2012), each term of the budgets of u, v and K_H was computed as the difference between the results from the simulations with and without orography in order to separate the contribution of the AP gravity wave from that of other synoptic processes of non-orographic origin, and averaged horizontally on the entire inner domain. The resulting domain-averaged differential terms of the budgets of u, v and K_H were then averaged vertically from 0 to 40 km, that is, box-averaged, in order to quantify the box-averaged dynamical influence of the simulated AP gravity wave.

Concerning the horizontal wind, it was found that the simulated AP gravity wave was associated with a pressure drag below 2 km that was counterbalanced by a wave-induced vertical transport of momentum from the flow above 15 km, that is, the vertical divergence of momentum flux was accelerating (decelerating) the flow below 2 km (above 2 km, especially above 15 km), which is a well-known mountain wave dynamical influence (e.g. Durran and Klemp, 1995; Héreil and Stein, 1999). The downward transport of momentum was also associated with a supply (sink) of momentum at the lateral boundaries of the inner domain, that is, accelerating (decelerating) horizontal divergence of momentum flux above (below) 2 km, suggesting that the simulated AP gravity wave had some dynamical influence on scales larger than that of the horizontal domain used for the budget, that is, 1500 km $\times$ 2580 km, thus confirming the remote effect of gravity wave forcing proposed by Durran and Klemp (1995) and Héreil and Stein (1999). It was further claimed that in a box of 1500 km $\times$ 2580 km horizontal size extending vertically from 0 to 40 km, one part of the vertical transport of momentum triggered by the simulated AP gravity wave induced a geostrophically balanced deceleration of the averaged inner flow, another part generated an ageostrophic circulation, that is, the secondary inertia–gravity wave discussed above, a third part triggered a momentum transfer with the larger scales at the lateral boundaries of the box and a last part resulted in a momentum transfer with the atmosphere above 40 km, consistent with the expectation that gravity waves significantly influence the large-scale dynamics of the middle atmosphere (e.g. Fritts and Alexander, 2003).

Concerning the horizontal kinetic energy, it was found that the simulated AP gravity wave enhanced frictional dissipation of energy above 15 km in association with enhanced turbulence in wave-induced convectively overturning regions in the stratosphere, an effect that was rather negligible in the budget of horizontal wind but not in the budget of K_H. It was then found that in the domain- and box-averaged budget, the decrease of K_H,

the turbulent dissipation and the transfer of kinetic energy to the flow above 40 km were balanced by a strong supply of kinetic energy from the potential energy of the inner flow and a two times smaller supply of kinetic energy from the outer flow at the lateral boundaries of the box. It was finally emphasised that the baroclinic production of kinetic energy, that is, supply of kinetic energy from the potential energy, was the effect of the ageostrophic circulation, that is, the secondary inertia–gravity wave.

In continuing this work, the budget analysis could be applied to various case studies of mountain waves at different scales, in order to draw a general picture of atmospheric processes associated with mountain wave forcing, at least from the model point of view. It should be emphasised at this point that comparisons with observations are essential to focus on the most realistic numerical experiment. Detailed analyses of absolute vorticity (e.g. Fritts et al., 1999) or/and PV (Chen et al., 2007) would certainly be more adapted to study the gravity wave's dynamical impact on large-scale circulations such as the polar vortex in the present case. Global modelling could also be used to investigate more properly the gravity wave large-scale impact, that is, without the scale restriction of regional modelling, on the long term for example (e.g. Watanabe et al., 2008). It is then questionable if the wave-induced small-scale processes impacting the large scales were realistically resolved at the 6-km (300 m) horizontal (vertical) resolution used here, and it is expected that future modelling studies involving always better computer performance will further address this topic. Finally gravity waves may have different sources than topography, such as convection, wind shear, geostrophic adjustment, body forcing or wave–wave interaction (e.g. Fritts and Alexander, 2003; Zülicke and Peters, 2006), and separating unambiguously the contribution of such gravity waves in a numerical experiment remains a challenge (e.g. Réchou et al., 2013).

6. Acknowledgements

The Swedish Research Council Grant 621-2010-3218 has funded this project. The WRF numerical experiments presented in this study were run at the High Performance Computing Center North (HPC2N, http://www.hpc2n.umu.se/). I thank Mats Lupsa who provided valuable tips to facilitate the data processing with Matlab, two reviewers for their beneficial comments on a former version of the manuscript, another reviewer for his constructive suggestions on the new version and Dr. Abdel Hannachi, the editor, for having supervised this review process.

References

Andrews, D. G. and McIntyre, M. E. 1976. Planetary waves in horizontal and vertical shear: the generalized Eliassen-Palm relation and the mean zonal acceleration. *J. Atmos. Sci.* **33**, 2031–2048.

Arnault, J. and Kirkwood, S. 2012. Dynamical influence of gravity waves generated by the Vestfjella Mountains in Antarctica: radar observations, fine-scale modelling and kinetic energy budget analysis. *Tellus A.* **64**, 17261. DOI: 10.3402/tellusa.v64i0.17261.

Arnault, J. and Roux, F. 2009. Case study of a developing African easterly wave during NAMMA: an energetic point of view. *J. Atmos. Sci.* **66**, 2991–3020.

Chen, C.-C., Hakim, G. J. and Durran, D. R. 2007. Transient mountain waves and their interaction with large scales. *J. Atmos. Sci.* **64**, 2378–2400.

Chou, M.-D., and Suarez, M. J. 1994. An efficient thermal infrared radiation parameterization for use in general circulation models. *NASA Tech. Memo.* 104606. **3**, 85 pp.

Durran, R. D. and Klemp, J. B. 1983. A compressible model for the simulation of moist mountain waves. *Mon. Wea. Rev.* **111**, 2341–2361.

Durran, R. D. and Klemp, J. B. 1995. Do breaking mountain waves decelerate the local mean flow? *J. Atmos. Sci.* **22**, 4010–4032.

Fritts, D. C. and Alexander, M. J. 2003. Gravity wave dynamics and effects in the middle atmosphere. *Rev. Geophys.* **41**(1), 1–64.

Fritts, D. C., Arendt, S. and Andreassen, Ø. 1999. The vorticity dynamics of instability and turbulence in a breaking internal gravity wave. *Earth Planets Space.* **51**, 457–473.

Héreil, P. and Stein, J. 1999. Momentum budgets over idealized orography with a non-hydrostatic anelastic model. I: two-dimensional flows. *Quart. J. Roy. Meteor. Soc.* **125**, 2019–2051.

Hong, S.-Y., Dudhia, J. and Chen, S.-H. 2004. A revised approach to ice microphysical processes for the bulk parameterization of clouds and precipitation. *Mon. Wea. Rev.* **132**, 103–120.

Hong, S.-Y., Noh, Y. and Dudhia, J. 2006. A new vertical diffusion package with an explicit treatment of entrainment processes. *Mon. Wea. Rev.* **134**, 2318–2341.

Kain, J. S. 2004. The Kain–Fritsch convective parameterization: an update. *J. Appl. Meteor.* **43**, 170–181.

Kinoshita, T., Tomikawa, Y. and Sato, K. 2010. On the three dimensional residual circulation and wave activity flux of the primitive equations. *J. Met. Soc. Jap.* **88**, 373–394. DOI: 10.2151/jmsj.2010–307.

Klemp, J. B., Skamarock, W. C. and Dudhia, J. 2007. Conservation split-explicit time integration methods for the compressible nonhydrostatic equations. *Mon. Wea. Rev.* **135**, 2897–2913.

Lilly, D. K. 1972. Wave momentum flux – A GARP problem. *Bull. Amer. Meteor. Soc.* **53**, 17–23.

Lilly, D. K. and Kennedy, P. J. 1973. Observations of a stationary mountain wave and its associated momentum flux and energy dissipation. *J. Atmos. Sci.* **30**, 1135–1152.

Lorenz, E. N. 1955. Available potential energy and the maintenance of the general circulation. *Tellus.* **7**, 157–167.

Mlawer, E. J., Taubman, S. J., Brown, P. D., Iacono, M. J. and Clough, S. A. 1997. Radiative transfer for inhomogeneous

atmosphere: RRTM, a validated correlated-k model for the long- wave. *J. Geophys. Res.* **102**(D14), 16663–16682.

Plougonven, R., Hertzog, A. and Teitelbaum, H. 2008. Observations and simulations of a large-amplitude mountain wave breaking over the Antarctic Peninsula. *J. Geophys. Res.* **113**, D16113. DOI: 10.1029/2007JD009739.

Réchou, A., Arnault, J., Dalin, P. and Kirkwood, S. 2013. Case-study of stratospheric gravity waves of convective origin over Arctic Scandinavia – VHF radar observations and numerical modelling, *Ann. Geophys.* **31**, 239–250. DOI: 10.5194/angeo-31-239-2013.

Scavuzzo, C. M., Lamfri, M. A., Teitelbaum, H. and Lott, F. 1998. A study of the low-frequency inertio–gravity waves observed during the Pyrénées Experiment. *J. Geophys. Res.* **103**, 1747–1758.

Skamarock, W. C. and Klemp, J. B. 2008. A time-split nonhydrostatic atmospheric model for weather research and forecasting applications. *J. Comp. Phys.* **227**, 3465–3485.

Spiga, A., Teitelbaum, H. and Zeitlin, V. 2008. Identification of the sources of inertia–gravity waves in the Andes Cordillera region. *Ann. Geophys.* **26**, 2551–2568.

Vadas, S. L., Fritts, D. C. and Alexander, M. J. 2003. Mechanisms for the generation of secondary waves in wave breaking regions. *J. Atmos. Sci.* **60**, 194–214.

Watanabe, S., Kawatani, Y., Tomikawa, Y., Miyazaki, K., Takahashi, M. and Sato, K. 2008. General aspects of a T213L256 middle atmosphere general circulation model. *J. Geophys. Res.* **113**, D12110. DOI: 10.1029/2008JD010026.

Zülicke, C. and Peters, D. H. W. 2006. Simulation of inertia–gravity waves in a poleward breaking Rossby wave. *J. Atmos. Sci.* **63**, 3253–3276. DOI: 10.1175/JAS3805.1.